Thrusting, exhumation, and basin fill on the western margin of the South China block during the India-Asia collision

Kai Cao, Philippe Leloup, Guocan Wang, Wei Liu, Gweltaz Mahéo, Tianyi Shen, Yadong Xu, Philippe Sorrel, Kexin Zhang

Thrusting, exhumation and basin fill on the western margin of the South China block during the India-Asian collision

Kai Cao[1, 2*], Philippe Hervé Leloup[3], Guocan Wang[1, 2], Wei Liu[1], Gweltaz Mahéo [3], Tianyi Shen[1, 2], Yadong Xu[4], Sorrel Philippe[3], Kexin Zhang[4]

[1] Hubei Key laboratory of Critical Zone Evolution, School of Earth Sciences, China University of Geosciences, Wuhan 430074, China
[2] Center for Global Tectonics, State Key Laboratory of Geological Processes and Mineral Resources, China University of Geosciences, Wuhan 430074, China
[3] Laboratoire de Géologie de Lyon: Terre, Planètes et Environnement, CNRS, Université de Lyon, 2 rue Daphaël Dubois, Villeurbanne 69622, France
[4] School of Earth Sciences, State Key Laboratory of Biogeology and Environmental Geology, China University of Geosciences, Wuhan 430074, China

*Corresponding author: Kai Cao, E-mail address: kai.cao@cug.edu.cn

Word count: 8398; Abstract: 434; Figures: 9; Table: 1; Appendixes: 8.

Abstract

The pattern and timing of deformation in southeast Tibet resulting from the early stages of the India-Asian collision, are crucial to understand the growth of the Tibetan Plateau but remain poorly constrained. Detailed field mapping, structural analysis, geochronological and thermochronological data along a 120 km section of the Ludian-Zhonghejiang (LZ) fold-thrust belt bounding the Jianchuan basin in western Yunnan, China document the Early Cenozoic tectonic evolution of the conjunction between the Lanping-Simao and South China blocks. The study area is cut by two major southwest-dipping brittle faults named Ludian-Zhonghejiang fault and Tongdian fault from east to west. Numerous kinematic indicators and the juxtaposition of Triassic meta-sedimentary rocks on top of Paleocene strata indicate thrusting along the Ludian-Zhonghejiang fault. Similarly, structural analysis shows that the Tongdian fault is a reverse fault. Between these structures, fault-bounded Permo-Triassic and Paleocene rocks are strongly deformed by nearly vertical and upright southwest-vergent folds with axes that trend nearly parallel to the traces of the main faults. Zircon and apatite (U-Th)/He and apatite fission track data from a Triassic pluton with zircon U-Pb ages of 225-237 Ma in the hanging wall of the Ludian-Zhonghejiang fault assisted by inverse modeling reveal two episodes of accelerated cooling during 125-110 Ma and 50-39 Ma. The Cretaceous cooling event was probably related to crustal thickening during the collision between the Lhasa and Qiangtang terranes. The accelerated exhumation during 50-39 Ma is interpreted to record the lifespan of the fold-thrust belt. This timing is corroborated by the intrusive relationship of Eocene magmas of ~35-36 Ma dated by zircon U-Pb into the fold-thrust belt. Early Cenozoic activity of the deformation system controlled deposition of alluvial-fan and braided-river sediments in the Jianchuan basin evidenced by eastward and northeastward paleoflows and terrestrial clasts derived from the hanging wall of the Ludian-Zhonghejiang thrust. Since 39 Ma, decreasing cooling rates likely reflects cessation of the fold-thrust belt. Early Cenozoic compressive deformation on the western margin of the South China block, together with geological records of contraction in central, northern and eastern Tibet, document Eocene upper crustal shortening located in the Himalaya, Qiangtang terrane and northern plateau margins together with contractional basin development intervened by Lhasa, Songpan-Garze and Kunlun terranes, coevally with or shortly after the onset of the India-Asian collision. This suggests that moderate crustal shortening affected a large part of Tibet in a spaced way contrary to homogenous crustal thickening soon after the collision, prior to the main crustal thickening propagated progressively from south to north. This complex deformation pattern illustrates the complexity of the Asian crustal rheology that contrasts with what were assumed in the existing geodynamic models.

Keywords: India-Asian collision, South China, Jianchuan basin, fold-thrust belt, low temperature thermochronology, lithospheric rheology

1. Introduction

The collision between India and Asia, which started since 60-50 Ma (Allègre et al., 1984; Ding et al., 2016; Hu et al., 2016; Najman et al., 2010; Rowley, 1996), has resulted in double-thickness crust and growth of the Tibetan Plateau that stands as a mean elevation of 5 km over a distance of ~2000 km north of the plate boundary. The reconstruction of the appropriate rheology of the Asian continental lithosphere as inferred from geodynamic models is crucial to understand the uplift and growth history of the Tibetan Plateau that have puzzled the earth scientists for a century (see reviews in Yin and Harrison (2000) and Kapp and Decelles (2019)). The prevailing models encompass 1) homogenous shortening and thickening distributed within Tibetan lithosphere analogue to a viscous sheet (Dewey and Burke, 1973; England and Houseman, 1986), 2) homogenous crustal thickening followed by flow of low-viscosity lower crust driven by topographic load (Bird, 1991; Clark et al., 2005; Clark and Royden, 2000; Royden et al., 1997), and 3) upper crustal shortening and oblique intracontinental subduction between coherent elasto-plastic lithospheric blocks (Meyer et al., 1998; Tapponnier et al., 1982, 1990). The first two models predict that uplift and deformation of the Tibetan plateau commenced throughout the plateau synchronously with or shortly after the India-Asian collision, while the third one predicts stepwise growth of the plateau from south to north and crustal deformation mostly localized along the boundaries of the lithospheric blocks. The discrimination of the three models largely depends on the quantification of the spatiotemporal evolution of intracontinental deformation resulting from the India-Asian collision and convergence. The middle-late Cenozoic extrusion of the crustal materials to the Tibetan sideways, inferred from plasticine analogue modeling, has been relatively well documented by structural analyses and geo-thermochronology (e.g., Tapponnier et al., 1976, 1982; Leloup et al., 1993, 1995, 2001; Cao et al., 2011; Lin et al., 2009; Zhang et al., 2010, 2011, 2014; Zhang et al., 2015, 2017). In contrast, how the Tibetan plateau crust deformed in the early Cenozoic remains poorly constrained (e.g., Cao et al., 2013; Clark et al., 2010; Horton et al., 2002; Leloup et al., 2012; Spurlin et al., 2005; Staisch et al., 2016; Tong et al., 2017; Yin and Harrison, 2000). Quantitative data of the geometry and kinematics of the first-order structures that predated the occurrence of the crustal extrusion within the collision belt are lacking.

Southeast Tibet is characterized by extrusion tectonics accommodated by large-scale strike-slip fault systems in middle-late Cenozoic times especially along the Ailao Shan-Red River shear zone (ASRR) and Red River fault (e.g., Tapponnier et al, 1976, 1982, 1990; Leloup et al., 1995, 2001) and is thus an ideal region to address the above question. However, the tectonic configuration of southeast Tibet prior to extrusion remains poorly understood. Deformed Paleogene sediments in southeast Tibet provide an opportunity to study Early Cenozoic sedimentation and deformation. The Jianchuan basin, one of the largest hinterland basins in southeast Tibet (Fig. 1), is proximal to the Red River fault and has been the subject of several recent studies pertaining to its age, deformation, exhumation and paleoelevation (Cao et al., 2019; Gourbet et al., 2017; Hoke et al., 2014; Li et al., 2015; Sorrel et al., 2017; Wei et al., 2016; Wissink et al., 2016; Wu et al., 2018; Yang et al., 2014). Despite its importance, the geodynamic context of its formation and the subsidence mechanisms are still poorly known.

In this study, our field and analytical data provide first quantitative constraints on the geometry, kinematics and timing of the compressive deformation along a fault zone that we termed Ludian-Zhonghejiang fold-thrust belt (LZTB) on the western margins of the South China block, western Yunnan, which preceded sinistral motion of the ASRR. These results allow establishing casual links between Early Cenozoic thrusting-induced rock exhumation within the deformation zone and deposition in the Jianchuan basin. Accordingly, we provide mechanistic interpretations for tectonic deformation and sedimentation in southeast Tibet corresponding to the India-Asian collision.

2. Geological setting

2.1 Regional tectonics

The southeast Tibetan Plateau comprises a collage of several major lithospheric fragments, including the Songpan-Garze, Lanping-Simao, Indochina and South China (Fig.1a). This region has experienced a protracted tectonic history from Paleozoic amalgamation to Mesozoic Tethys evolution (e.g., Burchfiel and Chen, 2012; Deng et al., 2014a; Jian et al., 2009a, b; Metcalfe, 2006), overprinted by

significant Cenozoic intracontinental deformation under the compound effects of India-Asian convergence and Pacific-Indonesian subduction (e.g., Burchfiel and Chen, 2012; Deng et al., 2014b; Leloup et al., 1995; Yin, 2010). Paleozoic-Mesozoic orogenesis in southeast Tibet is largely related to the evolution of the Paleo-Tethys recorded by numerous NS-striking belts of Devonian-Permian ophiolites and accretionary mélange complex (Burchfiel and Chen, 2012; Jian et al., 2009a, b). Large volume of Permo-Triassic plutonic and volcanic assemblages between the South China and Lanping-Simao blocks had been produced by westward subduction and final suturing of the Paleo-Tethys along the Jinsha-Ailao Shan suture zone (Burchfiel and Chen, 2012; Deng et al., 2014a; Faure et al., 2014; Jian et al., 2009a, b; Zi et al., 2012, 2013).

Since initial collision of the India with Asia at 60-50 Ma (Allègre et al., 1984; Ding et al., 2016; Hu et al., 2016; Najman et al., 2010; Rowley, 1996), the eastern margin of the Tibetan Plateau was strongly deformed, with early Cenozoic crustal shortening (Tapponnier et al., 2001; Spurlin et al., 2005; Studnicki-Gizbert et al., 2008; Tong et al., 2017) followed by southward block extrusion and rotation via large-scale strike slip faults (e.g., the ASSR; Fig.1; Tapponnier et al., 1982, 1990; Cao et al., 2011; Leloup et al., 1993, 1995, 2001; Lin et al., 2009; Tong et al., 2016; Zhang et al., 2010, 2011, 2014; Zhang et al., 2015, 2017). Early Cenozoic crustal deformation in east Tibet has been recorded by magmatism (Spurlin et al., 2005; Wang et al., 2001; Zhang et al., 2010), tectonic activity of fold-thrust system (Horton et al., 2002; Spurlin et al., 2005), deposition of syn-tectonic Paleogene basins, such as the Yushu-Nangqian and Gonjo basins (Horton et al., 2002; Spurlin et al., 2005; Studnicki-Gizbert et al., 2008; Tang et al., 2017) and paleomagnetism (Tong et al., 2017; Zhang et al., 2018). Recent thermochronological results from two vertical profiles at Deqin and Weixi in southeast Tibet reveal two episodes of rapid exhumation during 120-80 Ma and 60-40 Ma to the northwest of the Jianchuan basin (Liu-Zeng et al., 2018).

The middle-late Cenozoic crustal deformation in southeast Tibet is characterized by large-scale strike-slip fault system. Amongst them, the nearly-1000 km long ASRR extending from Vietnam to southeast Tibet defines a prominent crustal discontinuity and separates the South China to the northeast from Lanping-Simao/Indochina to the southwest. This shear zone comprises four narrow segments of strongly deformed metamorphic rocks: Day Nui Con Voi, Ailao Shan, Diancang Shan and Xuelong Shan from southeast to northwest (Fig. 1). The onset timing for left-lateral shear of the ASRR remains controversial, ranging between ~34 and 28 Ma (Cao et al., 2011; Leloup et al., 1995, 2001, 2007; Palin et al., 2013; Zhang et al., 2014) to ~25 Ma (Searle et al., 2010), or even later than 21 Ma (Searle, 2006). Cessation of its left-lateral deformation occurred at ~17 Ma (Leloup et al., 2001). Since ~10-5 Ma, the dextral Red River fault almost followed the trace of the ASRR (Leloup et al., 1995; Replumaz et al., 2001).

2.2 Subsidence and uplift history of the Jianchuan basin

The Jianchuan basin is a Paleogene intermontane basin in southeast Tibet on the South China block, mostly standing at an elevation of 3-4 km (Figs. 1 and 2). It is bounded to the west by the Qiaohou thrust belt (Gourbet et al., 2017). Paleogene sediments are strongly folded in the vicinity of the Ludian-Zhonghejiang fault, the eastern branch of the fold belt (Fig.2). To the northeast of the basin, basal sediments of the Paleogene Baoxiangsi Fm. (E_2b) rest unconformably on the Proterozoic and Paleozoic basement rocks. To the southeast of the basin, Eocene sediments are bounded by the Jianchuan normal fault, which belongs to a releasing bend of the Red River fault system that probably initiated in the Late Miocene (Leloup et al., 1995; Replumaz et al., 2001). The Paleogene sediments in the Jianchuan basin and surrounding areas stand unconformably on folded Triassic and older basement rocks (Burchfiel and Chen, 2012). Basin stratigraphy was recently reappraised based on new results of geological mapping, geochronologic data and fossil assemblages (Gourbet et al., 2017; Wu et al., 2018). Revised stratigraphic sequences of the Paleogene basin consist of the Mengyejing Formation "(Fm.)" (E_1m), Baoxiangsi Fm. (E_2b), Jiuziyan Fm. (E_2jz), Shuanghe Fm. (E_2s) and Jianchuan Fm. (E_2jc) from the bottom to the top (Fig. 3).

The Mengyejing Fm. (E_1m), outcropping in the southern part of the basin, is dominated by red mudstones and siltstones, with limited presence of sandstone and conglomerate layers (Fig. 2). These

sediments are interpreted to be a flood plain environment with local occurrence of alluvial-fan deposits (Gourbet et al., 2017). The Baoxiangsi Fm. (E_2b) having a thickness of up to ~600 m is exposed parallel to the bounding Ludian-Zhonghejiang fault to the west and occupies the greatest volume of basin infill (Gourbet et al., 2017; Fig. 3). This formation can be subdivided into two units: E_2b1 and E_2b2. The sediments of E_2b1 are characteristics of basal conglomerates, filling an uneven paleo-relief carved within the Shigu metamorphic schists along the northeast basin margin (Studnicki-Gizbert, 2006), indicative of an angular unconformable contact of the Baoxiangsi Fm. (E_2b) above the Proterozoic to Paleozoic metamorphic rocks (Fig. 2). This suite of sediments (E_2b1) also locally appear along the Ludian-Zhonghejiang fault (e.g., at site CD522 and east of site CD144; Figs. 2 and 4). Contrary to what was described by Wei et al. (2016), there is no clear field evidence for an angular unconformity between the E_2b1 and the underlying E_1m (Gourbet et al., 2017). Most of the Baoxiangsi Fm. (E_2b2) consists of massive red siltstones interbedded with red sandstones, containing parallel and cross bedding and channel-fill conglomerates, consistent with a facies interpretation of a braided river system, while the base of the sedimentary succession is locally made of massive, well-sorted, thick multi-storey channel-fill sandstones. There is no precise age control for both the Mengyejing Fm. (E_1m) and Baoxiangsi Fm. (E_2b). The presence of Paleocene-Early Eocene ostracods in the Mengyejing Fm. (E_1m), along with charophyte assemblages and Late Eocene mammalian faunas in the Baoxiangsi Fm. (E_2b), allow roughly attributing Paleocene and Eocene ages to these two formations respectively (BGMRY, 1990). This timing assignment is supported by the cut-off relationships between 35-36 Ma old intrusive rocks and the sediments of the Mengyejing (E_1m) and Baoxiangsi Fms. (E_2b) (Fig. 3; Gourbet et al., 2017).

The overlying deposits of the Jiuziyan Fm.(E_2jz), Shuanghe Fm. (E_2s) and Jianchuan Fm. (E_2jc) appear to be restricted to the eastern part of the Jianchuan basin (Fig. 2). The 0-100 m-thick Jiuziyan Fm. (E_2jz) seems limited to the northeastern corner of the basin, mostly resting on the mountain top and isolated by incision of the river network (Fig.2). The Jiuziyan Fm. (E_2jz) is locally in an erosional basal contact above the red mudstones of the Mengyejing Fm. (E_1m), while the sediments show a regular transition without any clear angular unconformity at some spots (Gourbet et al., 2017). It consists of multi-storey carbonate successions, including life-position stromatolites interbedded with massive matrix-supported conglomerates and argillaceous calcisiltites, indicative of a palustrine-lacustrine environment (Sorrel et al., 2017). The 0-200 m-thick Shuanghe Fm. (E_2s), overlying conformably the Jiuziyan Fm. (E_2jz), is composed of poorly consolidated yellow sandstones, interbedded with organic-rich coal levels, as well as few layers of lava, tuff and volcanoclastic sediments. The sediments are commonly cut by intrusions (mostly lamprophyres), often sills in the coals or along sandstones stratifications. The strata are folded under nearly EW-directed contraction (Gourbet et al., 2017). The 0-300 m thick Jianchuan Fm. (E_2jc) overlies the folded sediments of the Shuanghe Fm. (E_2s). These strata are dominantly volcanoclastic and relates to Late Eocene intrusion of the Shamao Shan syenite (Gourbet et al., 2017). The deposition timing of the Shuanghe Fm. (E_2s) and Jianchuan Fm. (E_2jc) was recently refined to be at ~35.9±0.9 Ma and 35.4±0.8 Ma respectively, from zircon U-Pb and $^{40}Ar/^{39}Ar$ dating on interbedded and crosscutting igneous rocks (Fig. 3; Gourbet et al., 2017). This is supported by newly-discovered fossils of chara and ostracod (Wu et al., 2018). The age of the Shuanghe Fm. (E_2s) is further corroborated by a jaw (found in coal deposits) of a large amynodontid that thrived during the Late Eocene Ergilian interval (37.2-33.9 Ma) (Gourbet et al., 2017).

The elevation history of the Jianchuan basin remains highly debated. Paleoaltimetry reconstructions based on stable isotopes suggest an attainment of modern surface height of ~3.3±0.5 km asl. in the Late Eocene for the Jianchuan basin (Hoke et al., 2014). Similar work on the Shuanghe Fm. (E_2s) suggests that the Jianchuan basin had reached ~2.6 km asl. close to modern surface elevation in the Late Eocene (Li et al., 2015). However, the Shuanghe Fm. (E_2s) was recently revised to be Late Eocene in age, and basin elevation was also re-evaluated to indicate a lower elevation of ~1.2±1.2 km asl. (Gourbet et al., 2017). Recent stable isotope and fossil pollen coexistence data suggest the Jianchuan basin experienced a gradual uplift from between 0.5 km asl. and 2.5±0.7 km asl. during deposition of the Jiuziyan Fm. (E_2jz) to between 0.9 km asl and 2.9±0.6 km asl. during deposition of the Shuanghe Fm. (E_2s) (Wu et al., 2018). Low temperature thermochronology data interpreted in the light of thermal modelling suggest that the Jianchuan basin experienced 2.3-3.2 km of rapid exhumation at a rate of 0.57-0.80 mm yr^{-1} between ~28 and 20 Ma (Cao et al., 2019). These results allowed us to link pronounced relief generation

of southeast Tibet during the Oligocene-Early Miocene to thrusting in the context of regional NW-SE crustal shortening (Cao et al., 2019).

3. Geological mapping

The geometry, kinematics and timing of Cenozoic deformation of the Jianchuan basin and adjacent area have remained debated (Burchfiel and Chen, 2012; Deng et al., 2014b; Gourbet et al., 2017; Leloup et al., 1993; Tang et al., 2016; Wang et al., 1998; Yang et al., 2014). New mapping results on the western flank of the Jianchuan basin (Figs. 2 and 4) indicate that this area is predominantly affected by NNW-striking, WSW-dipping brittle thrusts separating narrow panels of Permo-Triassic and Paleocene strata. These panels are deformed by upright and tight folds with axes subparallel to the trend of the main faults. These structures define a fold-thrust belt that lacks detailed descriptions and quantitative constraints in Yang et al. (2014) and tentatively named "Qiaohou thrust belt" in Gourbet et al. (2017). In order to avoid confusion with the dextral strike-slip Qiaohou fault that is considered as a part of the active Red River fault system (Allen et al., 1984; Leloup et al., 1995), we use the new term Ludian-Zhonghejiang fold-thrust belt (LZTB) instead of "Qiaohou thrust belt". The fold-thrust belt consists of two main thrusts: the Tongdian and Ludian-Zhonghejiang faults and several parallel folds (Figs. 2 and 4). The following sections present the mapping results that focus on geology of the central and southern portions of the Ludian-Zhonghejiang fold-thrust belt, NE-trending faults and Qiaohou fault, as well as folded lithologic units along three main transects A-B, B'-C and E-F (Fig. 4).

3.1 Ludian-Zhonghejiang fold-thrust belt (LZTB)

The LZTB stretches over 120 km between the Xuelong Shan and Diancang Shan metamorphic gneiss belts (Fig. 1) along a zone used to be called "Madeng gap", where no high-grade metamorphic rocks are related to the ASRR (Leloup et al., 2001). The 7-12 km wide deformation zone involves Permo-Triassic sedimentary and volcanic rocks in the hanging wall, as well as Paleogene terrestrial sediments of the Jianchuan basin in the footwall (Fig. 4). The northern part of the fold-thrust belt is poorly defined due to heavy vegetation, but the principal fault still can be identified based on field observations of prominent topographic relief and intensively folded Eocene sediments proximal to the fault trace. In contrast, the central segment of the fold-thrust belt outcrops well and is thus the target of our detailed mapping.

3.1.1 Ludian-Zhonghejiang fault and Paleogene strata

The Ludian-Zhonghejiang fault brings Triassic strata on top of the Eocene Baoxiangsi Fm. (E_2b; Figs. 2 and 4). To the east of the fault, the Baoxiangsi Fm. (E_2b) is dominated by thick-bedded red medium-grained lithic sandstone interbedded with lenticular layers of conglomerates that are poorly-sorted, grain-supported, sub-rounded, and display scour-and-fill and cross bedding structures. This unit is interpreted as an alluvial fan fed by a braided river proximal to a local topographic gradient (Gourbet et al., 2017).

The Ludian-Zhonghejiang fault (LZF) is a NNW-SSE-striking and west-dipping thrust fault (Fig. 2). Folding is more intense on either side of the fault zone than it is further away, indicative of localized deformation along the contact between the Triassic and Paleogene strata. The fault has locally a complex trace (Fig. 4). At sites S277 and S219, a fault striking N92E brings the Triassic rocks on top of the Eocene red beds (Figs. 5a and 5m). At site CD335/CD435, faults with various orientations bring the Triassic rocks atop the Eocene sediments (Figs. 5b, 5c and 6a). The main fault contact in general trends NW-SE and dips to the SW, but is locally close to horizontal, gently dipping to the south, or even to the SE (Fig. 6a). This results in a complex shape of contact between the Triassic and Paleogene units. The primary fault appears as a low angle thrust nappe affected by latter deformation. The fault contact bears striations (Figs. 5d and 5e) but with various orientations, which prevents to define a clear common direction of motion for the thrusting (Fig. 6a). The intrusive relationship of a late Eocene lamprophyre with the main thrust fault is ambiguous (Figs. 5b and 5c). However, the intrusion clearly cut across the schistosity parallel to the thrust affecting the Triassic rocks (Fig. 5f), suggesting that the intrusion postdated the thrusting. This observation is also supported by the intrusion of a late Eocene syenite within the LZF at site CD321 (Fig. 4). The Eocene and Triassic sediments are folded and affected by later faults (Figs. 6a-c). Some of these faults are parallel to the main contact, but others are ~N80° to

N120° trending dextral faults (Fig. 6c). As this later set of faults cartographically crosscuts the contact between the Eocene and Triassic sediments (Fig. 4), we interpret them as resulting from a SE-NW compression after the thrust motion. At site CD237, Triassic coal-bearing slates above the nearly N-S-striking thrust are schistosed with S-C fabrics (Figs. 5g, 5h and 6b), suggesting top to the NE ductile-brittle thrusting (Figs. 5i-k). In contrast, sandstone beds of stronger competence at site CD333 show less ductile-brittle fabrics but are deformed, forming meter-scale asymmetric necked boudins (Fig. 5n).

Along transect E-F between the observation sites CD237 and CD522 (Fig. 5h), the Eocene strata dip almost vertically at the vicinity of the fault, but dip gradually more gently away from the fault. The vertical clastic layers proximal to the thrust fault are dominated by a mixture of very poorly-sorted, sub-angular to sub-rounded pebbles and boulders of limestone, sandstone and volcanic origin (Fig. 5l), indicative of debris flow and hyper-concentrated flood flow deposits. In general, the Eocene strata east of the fault are deformed by a set of open synclines with steep axial planes striking N-S to NW-SE (Figs. 2b, 6f and 6g). A section across the Paleogene sediments (mostly E_1m and E_2b) of the Jianchuan basin is typified by long-wavelength folds with one syncline showing a steep western limb adjacent to the thrust front (Fig. 2b). The axial traces of the folds within the E_2b2 are sub-parallel to the strike of the LZF (Figs. 6f and 6g). The Triassic clastic sediments (T_3s) are also strongly folded with fold hinge striking NNW (Fig. 6h), parallel to the fault trace of the LZF.

3.1.2 Tongdian fault and flanking units

West of the LZF, the Tongdian fault places folded late Permian clastic deposits over Triassic volcanic sequences (Fig. 4). To the west of the Tongdian fault, the rocks comprise a thick sequence of limestone interlayered with siltstone and mudstone of late Permian ages (Tang et al., 2016) that was originally considered to be Triassic in age (BGMRY, 1990). Limestone and marl are most common in the lower part of the unit that shows an overturned anticline at site CD524. In the upper part the strata contain more fine-grained clastic deposits of siltstone and mudstone. East of the Tongdian fault, the early to middle Triassic volcanic rocks ($T_{1-2}p$) consist of massive rhyolitic lava, dacitic lava, rhyolitic or dacitic breccias and tuff. In the northern end of the mapped area, these rocks are intruded by small bodies of Eocene syenite with irregular intrusive margins (Fig. 4). In general, this volcanic sequence is strongly fractured by discretely-spaced small scale secondary faults and abundant cleavages that trends S115-155° and dips SW60-86°(Fig. 6d). Locally, NE-dipping tuff layers are still distinguished in the lower part of the unit (Tang et al., 2016). The suite of Triassic volcanic rocks shows a nonconformable contact with the overlying Triassic clastic deposits (T_3s) to the east.

The Tongdian fault is a steeply dipping fault zone that locally strikes S130-160° and dips SW46-80° at sites CD517, CD518 and CD524 (Figs. 4, 5o and 5p). Striated surfaces within the fault zone show both top to the NE reverse slip and right slip (Fig. 6d) indicative of transpressional deformation. The late Permian strata are deformed by a set of open to tight, upright-plunging folds that trend NW nearly parallel to the bounding Tongdian fault (Fig. 6i), locally showing overturned limb compatible with a NE vergence (Fig. 4). At distances of <1 km from the Tongdian fault, the fold are recumbent and chevron folds less spaced than further away from the fault (Fig. 4), suggesting that the folds are genetically related to thrusting along the fault. Proximal to the Tongdian fault, the Triassic volcanic unit has well-developed cleavages (Fig. 5d) that strikes parallel to the principal fault planes, indicating localized deformation associated with the transpression.

At site CD516 ~500 m to the southwest of the Tongdian fault, a steeply dipping brittle fault strikes S140-180° and dips SW60-80° (Fig. 6d). Striations and chatter marks on the fault surfaces indicate both reverse slip and right slip (Fig. 6d). These suggest this fault to be a transpressional structure, which led to folding of the late Permian strata in its hanging wall (Figs. 4 and 6i). The similarity of geometry and kinematics of this fault to the Tongdian fault suggest that this fault is likely a branch fault of the Tongdian fault.

3.2 ENE-trending dextral strike-slip faults

Apart from thrust faults, we observed a set of ENE-trending, steeply dipping, brittle faults at several localities (e.g., CD241, CD320, CD327, CD328 and CD347; Figs. 4 and 6c). On the fault planes, nearly

horizontal calcite growth striae together with the asymmetric calcite crystallization marks indicate a dextral sense of shear. Besides, meters-scale of right lateral separation of Eocene conglomerate beds near site CD320 attests to dextral strike slip offset on the fault. Although the relationship between these ENE-striking right lateral faults with the fold-trust belt cannot be easily examined in the field, we infer that these faults could postdate the thrust structures based on the observations that the ENE-striking dextral strike slip faults apparently cut all the rocks involved in the LZTB and especially the Eocene Baoxiangsi Fm. (e.g., at site CD320; Fig. 4). More convincing evidences for this relationship would require more work.

3.3 Qiaohou fault

The Qiaohou fault was regarded as a part of the Red River fault system (Allen et al., 1984; Leloup et al., 1995). In the mapped area, this fault zone consists of two splays, named Qiaohou fault-1 and Qiaohou fault-2 respectively (Fig. 4). The Qiaohou fault-1 separates Eocene volcanic rocks in the west from late Permian siltstone and limestone to the east, between which a prominent topographic step occurs. Field measurements show that it is a NNE-striking, steeply dipping, brittle fault at site CD502 (Figs. 4 and 6e). Nearly horizontal striae and chatter marks on the fault planes indicate a sense of dextral strike slip with a minor normal component (Fig. 6e). Likewise, the Qiaohou fault-2 shares a similar geometry and kinematics with the Qiaohou fault-1. This fault splay bounds the eastern margin of the Quaternary Madeng basin and is presumably an active fault. These dextral faults are thus young structures that probably initiated in the Late Miocene or later (Allen et al., 1984; Leloup et al., 1995).

To sum up, field observations provide relative timing for the Cenozoic deformation in the study area based on cutoffs between the structures and Cenozoic sediments and Eocene magmas. Accordingly, we identified four Cenozoic deformation generations. The LZTB dominated the first deformation phase with top to the NE-directed thrusting that took place prior to the Late Eocene. The exact magnitude of crustal shortening across the LZTB is difficult to restore due to the paucity of constraints on the deep structure of the thrust belt. Subsequently, the Qiaohou fault being a part of the Red River system likely commenced in the Late Miocene or later (Allen et al., 1984; Leloup et al., 1995). The ENE-trending dextral strike-slip faults offset the fold-thrust belt, indicating that this set of faults postdated the thrusting, but their exact activity timing remains unknown. The latest deformation generation is typified by the Qiaohou fault-2, which could be an active fault controlling the Quaternary Madeng basin. Meanwhile, we do not exclude the existence of Pre-Cenozoic structures in this area, but it seems that they have been modified by Cenozoic deformation. In this paper, we thus concentrate on the geometry, kinematics, timing and implications of the first deformation generation expressed by the LZTB.

4. Sampling and analytical methods

In order to address the timing of deformation within the LZTB, we employed radiometric dating within the deformation zones (Fig. 2; Tables 1 and S1). On one hand, we collected 8 samples from syenitic plutons and lamprophyres intruding the fold-thrust belt for zircon U-Pb dating. These results will firmly place minimum age for the activity of the thrust belt. We also took 6 samples along a vertical profile in the Ludian pluton in the hanging wall of the LZF for multiple dating techniques, including zircon U-Pb, zircon (U-Th)/He (ZHe), apatite fission track (AFT) and apatite (U-Th)/He (AHe). The zircon U-Pb geochronology with closure temperature of 750±50 °C (Cherniak et al., 2004) resolves the crystallization age of the igneous rocks. By contrast, the combination of lower-temperature thermochronological systems of ZHe, AFT and AHe with closure temperatures ranging from ~220 to 40 °C record the cooling path in the upper several kilometers of the crust (Reiners and Brandon, 2006). Together, these data analyzed with inverse thermal modeling, are able to constrain a complete thermal history of the rocks in the hanging wall of the LZF and further provide information on the onset, duration and rate of rock exhumation, which can be related to thrusting (Reiners and Brandon, 2006; Turab et al., 2017). Apatite and zircon aliquots were extracted from samples using standard crushing, magnetic and heavy-liquid separation techniques. Detailed analytical procedures for zircon U-Pb geochronology, apatite fission track and zircon and apatite (U-Th)/He are described in the supplementary material S1.

5. Results and interpretation

The analytical datasets are presented in Fig. 2 and Table 1, as well as supplementary material S1 and

Tables S1-S6.

5.1 Zircon U-Pb geochronology

The majority of dated zircon grains from Mesozoic igneous rocks with oscillatory zoning have low U/Th ratios of <10 (Table S2), indicative of igneous origin. Two samples CD144 and CD149 were collected from the Ludian granite in the hanging wall of the northern segment of the Ludian-Zhonghejiang fault (Fig. 2a). Most zircon grains yield concordant ages clustering at 208-252 Ma (Tables 1 and S2; Fig. S1a). Fifteen and nineteen age points from samples CD144 and CD149 give weighted mean U-Pb ages of 227.7±4.6 Ma and 234.5±4.7 Ma respectively (Figs. S1a and S1b). These two ages thus represent the crystallization age of the Ludian granite. The sample CD327 is a dacite collected in the Pangtiange Fm. ($T_{1\text{-}2}p$). Several ages are pre-Cenozoic, but the lower intercept defined by the linear regression of 10 ages clusters at two group ages at ~270 Ma and ~235 Ma (Tables 1 and S2; Figs. S1c and S1d). Seven out of ten zircon grains yield a younger weighted mean U-Pb age of 234.4±8.5 Ma, overlapping with published zircon U-Pb ages spanning from ~237 to 250 Ma in the same volcanic unit (Yang et al., 2014; Table S3).

Six samples CD316, CD323, CD325, CD330, CD331, CD335/CD435 were collected from some small porphyry dykes intruding in the LZTB in the northern end of the mapped area (Figs. 2 and 4). Of them, samples CD316, CD323 and CD331 have a few Cenozoic ages that are sub-concordant at ~34-36 Ma (Tables 1 and S4; Figs. S1e-j). Ten, five and six ages yield weighted mean U-Pb ages of 34.5±1.3 Ma, 34.3±1.6 Ma and 35.3±1.7 Ma for samples CD316, CD323 and CD331 respectively (Fig. S1; Tables 1 and S2). Samples CD335 and CD435 were taken from the same lamprophyre at site CD335, so we combined their zircon U-Pb data sets together. Most zircons from these two samples present large range of pre-Cenozoic ages spanning from 251 Ma to 2273 Ma. Six zircon grains yield a weighted mean U-Pb age of 35.1±0.5 Ma (Figs. S1k and S1l). The other two samples CD325 and CD330 yield much more inherited pre-Cenozoic ages (Figs. S1m-p). Only one grain per sample yield Eocene ages that may represent the intrusion age, but the points fall off the concordant curves and thus do not provide a robust age constraint. Overall, the late Eocene ages recorded by these samples generally overlap with previous zircon U-Pb data for the porphyry, granite and syenite plutons and dykes as well as volcanic clasts in and around the Jianchuan basin (Fig. 3 and Table S4), indicating a major flare-up event occurred from ~35.7 to 34.5 Ma (Gourbet et al., 2017).

5.2 Low-temperature thermochronology

Single-grain ZHe ages obtained from the samples CD144, CD145 and CD148 consistently cluster within ~100-140 Ma (Tables 1 and S5; Fig. 7a), significantly younger than the Triassic emplacement age of the Ludian granite. These ages thus reflect later cooling or exhumation event. Single-grain ZHe ages of samples CD145 and CD148 show reverse relationships with the effective uranium concentrations ([eU]=[U]+0.235*[Th]; Guenthner et al., 2013; Fig.7a), indicating that radiation damage affected the zircon grains (Guenthner et al., 2013).

Four single-grain AHe ages from the low-elevation sample CD145 range from 29.4 Ma to 43.6 Ma (Fig. 7b). Five single-grain ages from the high-elevation sample CD148 span from 36.0 Ma to 49.6 Ma. In general, neither positive nor negative relationships between the AHe ages and eU appear in Fig. 7b. The single-grain AHe ages of the sample CD148 overlaps with the AFT ages of CD148 and CD149 within errors at comparable elevations, but much younger than the corresponding ZHe ages, indicating self-consistency of the multiple thermochronology data. Two replicates from samples CD145 and CD148 yield very young ZHe ages probably because of grain loss during the preparation process. These two data were not used for inverse modeling and interpretation. The Eocene cooling ages broadly overlap with AHe ages from the northern part of the Ludian pluton (Liu-Zeng et al., 2018).

Five samples CD144, CD146, CD147, CD148 and CD149 from an elevation profile along the Ludian granite with sufficiently countable grains and kinetic parameters yield a cluster of Eocene AFT ages ranging from 35.8 Ma to 45.3 Ma (Tables 1 and S6). All ages passed the $P(\chi^2)$ test with very low dispersion values, indicative of single age populations (Galbraith and Green, 1990). The mean track lengths span from 13.35 to 14.01 μm (Table S6). AFT age plot against elevation show a general positive correlation (Fig.7c).

5.3 Thermal modeling

The cooling histories of the Ludian granite were further derived by using the Bayesian transdimensional Markov chain Monte Carlo protocol (Gallagher, 2012). The inverse scheme of this program is preferably designed to reconstruct thermal history from a thermochronological age-elevation profile. The model was set up taking into account all AFT ages, track length distribution and kinetic parameters, as well as acceptable single ZHe and AHe ages, apatite and zircon crystal dimensions and U, Th and Sm concentrations from samples CD144, CD145 and CD148. Fission track annealing and He diffusion algorithms used for ZHe, AFT and AHe modelling refer to Guenthner et al. (2013), Ketcham et al. (2007) and Gautheron et al., (2009), respectively.

In order to make the modeling informative and convincing, two independent geological boundary conditions were given: 1) samples collected from the Ludian granite are at the surface, and thus between 0 and 10 °C at present day; 2) a loosely constrained condition of a temperature of 300±50 °C at 110±20 Ma was given as a start. This constraint box forces the model to pass through the ZHe partial retention zone during the late Cretaceous based on reported Late Cretaceous rapid cooling event of the same batholith near Weixi ~100 km northwest of our samples (Liu-Zeng et al., 2018). We used the default values of 30 °C/km for the paleo and present geothermal gradients and allow the temperature offset to vary over time. Each 1,000,000 iterations were performed as burn-in and post-burn-in iterations. The optimized temperature-time curves present a four-episode cooling history (Fig. 7d). The first cooling stage at~125-110 Ma reflects a rapid exhumation process for the pluton passing through the ZHe partial retention zone (PRZ). The following cooling episode between 110-50 Ma shows the rock resided on the upper boundary of the ZHe PRZ for ~60 Ma. Notably, the subsequent accelerated cooling between ~50 and 39 Ma at a rate of ~9 °C Ma^{-1} (Fig. 7d) is interpreted as exhumation related to thrusting along the LZTB. Based on the modelled cooling histories, the temperature difference of the highest and lowest samples ranges from ~6 to ~12 °C (Fig. 7d). An elevation difference of ~400 m between these two samples thus infers geothermal gradients between ~15-30 °C km^{-1}. The cooling rate of the Ludian pluton between ~50-39 Ma translates to an apparent exhumation rate of ~0.3-0.6 mm a^{-1}. The relatively rapid exhumation ended at ~39 Ma and was followed by a protracted period of extremely slow cooling at a rate of <1.75 °C Ma^{-1} (Fig. 7d) indicative of the cessation of the deformation in the LZTB.

6. Discussion

6.1 Temporal and spatial constraints on the Ludian-Zhonghejiang fold-thrust belt

Geological crosscutting relationships provide relative chronology for the activity of the LZTB. For example, the intrusion of porphyry dykes of 35-36 Ma within the LZTB (Figs. 4, 5b and 5c) indicates that the LZTB was active prior to ~36 Ma. Likewise, the occurrence of syn-tectonic sediments of Baoxiangsi Fm. (E_2b) (see below) older than the Shuanghe Fm. dated at ~35.9±0.9 Ma (Gourbet et al., 2017) suggest that the deformation within the fold-thrust belt occurred no later than 36 Ma. Independently, rapid cooling of the Ludian pluton in the hanging wall of the LZF derived from thermochronology and inverse models are compatible with thrusting activity of the LZTB during 50-39 Ma. The existence of syn-tectonic sediments of the Baoxiangsi Fm. (E_2b) in the footwall of the thrust belt rules out regional uplift at that time span (See the detailed discussion in the next section), and thus implies NE-oriented crustal shortening initiated at 50 Ma and continued until 39 Ma on the western margin of the South China block. This robust temporal constraint is consistent with geological crosscutting observations. Since 39 Ma, the quiescence of the LZTB is supported by the deposition of sediments in low-lying and flat alluvial to palustrine and fluvial systems of the Jiuziyan and Shuanghe Fms. (Figs. 2 and 3; Gourbet et al., 2017; Sorrel et al., 2017) in the eastern part of the Jianchuan basin. In space, this fold-thrust system may extend to the northwest near Weixi county, where the onset of rapid exhumation during 60-40 Ma was interpreted as relating to the reactivation of local structures (Liu-Zeng et al., 2018). Further investigations on the fault extent and correlation are still needed.

6.2 Syn-tectonic deposition in the Jianchuan basin

The Jianchuan basin, filled by kilometers-thick Paleogene terrestrial sediments, has attracted much attention in order to understand the tectonic, paleoenvironmental and topographic evolution of southeast

Tibet. Despite its importance, how the basin did form remains unclear. Two sets of models have been proposed to explain the basin formation and evolution. In the first set of models, the alluvial-fan and braided-stream clasts of the Baoxiangsi Fm. were interpreted as deposits coeval with the ultrapotassic magmatism from 40 to 27 Ma in a rift setting (Wei et al., 2016), which was induced by intraplate extension related to the delamination of a thickened lithosphere (Chung et al., 1997). However, field evidences show that the deposition of the Shuanghe and Jianchuan Fms. (E_2s and E_2jc), rather than the Baoxiangsi Fm. (E_2b), was coeval with the magmatic episode that was restricted to a very short time between 35 and 36 Ma (Table S4; Gourbet et al., 2017; this study). Therefore, the argument for the deposition of the Baoxiangsi Fm. in a rift basin is not supported by the new stratigraphy of the Jianchuan basin. Furthermore, no normal fault of that age has been described up to now, neither within nor close to the Jianchuan basin. In the second model, Paleogene sedimentation in the Jianchuan basin was proposed to be simultaneous with basement uplift and thrusting in a regional NE-SW compression based on the existence of possible syn-depositional structures (e.g., mudstone dykes in the major thrust fault plane and diapirs in the fracture of hanging wall) in the thrust (Yang et al., 2014). This hypothesis seems partly consistent with local structural observations but lends no support from our observations on the architecture of the LZTB and the syn-depositional structures of the Jianchuan basin.

Our results suggest that deposition of the Baoxiangsi Fm. (E_2b) in the Jianchuan basin is syn-tectonic and closely related to the development of the LZTB during crustal shortening (Fig. 8) based on several lines of evidence. Field observations show that the sediments in the Baoxiangsi Fm. (E_2b) were predominately sourced from the hanging wall of the LZF. At the bottom of the Baoxiangsi Fm. (E_2b1), an abrupt appearance of massive basal conglomerates and up-section sandstones bearing cross bedding marks a significant change of sedimentary facies from flood plain (i.e., the Mengyejing Fm. (E_1m)) to alluvial fan and braided river (Fig. 3). This indicates prominent topographic relief generation triggered by the contractional deformation within the LZTB, which supplied large amounts of terrestrial clasts to the adjacent Jianchuan basin (Fig. 8). This inference is also corroborated by predominantly eastward and northeastward paleocurrents restored by measurements of pebble imbrications and cross beddings in the Baoxiangsi Fm. (Wei et al., 2016; Wissink et al., 2016; this study; Fig. 2). Apart from these, a combination of poorly-sorted, sub-angular to sub-rounded pebbles and boulders in the basal conglomerates are composed of limestone, sandstone and volcanic rocks (Fig. 5l), which were apparently derived from proximal Permo-Triassic lithologic units in the hanging wall of the LZF. We thus propose that sedimentation of the Baoxiangsi Fm. (E_2b) commenced since ~50 Ma and lasted until ~39 Ma, coevally with the duration of the crustal shortening in the LZTB. This timing is broadly in agreement with estimated Eocene age from fossil assemblages for the Baoxiangsi Fm. (BGMRY, 1990), overlain by deposition of the Jiuziyan Fm. (E_2jz), Shuanghe Fm. (E_2s) and Jianchuan Fm. (E_2jc) during the Late Eocene (Gourbet et al., 2017; Sorrel et al., 2017; Wu et al., 2018). Sedimentation during the Jiuziyan and Shuanghe Fms. (E_2jz and E_2s) likely took place in distal alluvial fan-deltas and sub-lacustrine (alluvial-lake) environments characteristics of low-lying depositional systems (Sorrel et al., 2017), which is congruent with the cessation of the fold-thrust belt and final infill of the Late Eocene intermontane Jianchuan basin.

6.3 Cretaceous-Early Cenozoic crustal deformation and uplift of the southeast Tibet and implications for the lithospheric rheology of the Tibet

Rapid Cretaceous cooling events have been revealed by thermochronometres in the east and southeast Tibet (Tian et al., 2014; Liu-Zeng et al., 2018). They most likely corresponded to crustal thickening as a result of the collision between the Lhasa and Qiangtang terranes implied from the geological records of central Tibet (Kapp et al., 2005, 2007). We follow this hypothesis to interpret rapid Cretaceous exhumation in the Jianchuan area recorded by our thermochronological data. However, the detailed geological processes in southeast Tibet during Lhasa-Qiangtang collisional orogenesis would need much more work. We focus here on Early Cenozoic deformation as discussed below.

A growing number of structural and paleomagnetic investigations suggest that southeast Tibet has been dominated by extrusion tectonics since the Late Eocene, which was predominantly accommodated by major strike slip faults along the block boundaries (Tapponnier et al., 1982; 1990; Cao et al., 2011; Leloup et al., 1993, 2001; Lin et al., 2009; Tong et al., 2016; Zhang et al., 2011, 2014), though some

551 others argued for a geodynamic model of lower crustal flow for Late Cenozoic surface uplift (Clark et
552 al., 2005; Ouimet et al., 2010; Royden et al., 1997, 2008; Schoenbohm et al., 2006; Wang et al., 2016).
553 Nevertheless, how regional crustal deformation in the Early Cenozoic was partitioned remains poorly
554 understood. Our results indicate that the western margin of the South China block was affected by NE-
555 directed compression since ~50 Ma nearly synchronous with the onset of the India-Asian collision,
556 which is expressed by compressive deformation in the LZTB and simultaneous sediment deposition in
557 the adjacent Jianchuan basin. The Permo-Triassic rocks were intensely deformed within the LZTB in a
558 pattern of tight and recumbent fold assemblages in a short wavelength and high amplitude between
559 major thrust faults (Fig. 2b). In contrast, the Eocene sediments in the Jianchuan basin show typical
560 broad, long-wavelength folds in the footwall of the LZF (Fig. 2b). The discrepancy of deformation
561 intensity between the basin and fold-thrust belt raise two questions of 1) whether southeast Tibet
562 attained its present-day height due to crustal shortening in the Eocene, and 2) how the strain propagated
563 to accommodate the India-Asian convergence.
564
565 The Eocene paleoaltimetry of southeast Tibet, taking the Jianchuan basin in northwest Yunnan as an
566 example, remains controversial. Previous studies argued that the Jianchuan basin has uplifted to an
567 elevation of ~3.3±0.5 km asl. (Hoke et al., 2014) or ~2.6 km asl. (Li et al., 2015) in the Eocene close
568 to a modern surface height, which was interpreted as resulting from crustal shortening in response to
569 the India-Asian collision (Li et al., 2015). However, recent work based on stable isotopes and fossil
570 pollen coexistence instead argue for a lower elevation for the Eocene basin ranging from ~1.2±1.2 km
571 asl. (Gourbet et al., 2017) to 0.9-2.9±0.6 km asl. (Wu et al., 2018). Our structural data suggest limited
572 uplift of the Jianchuan basin in the Eocene as follows. The long wavelength of the folds affecting the
573 Paleogene sediments (i.e., E_1m and E_2b) imply a small crustal shortening (less than 5 km estimated from
574 cross section in Fig. 2b) in the Jianchuan basin during the activity of the LZTB between ~50 Ma and
575 39 Ma. In addition, Late Eocene rocks (i.e., E_2jz, E_2s and E_2jc) restricted in the southeastern corner of
576 the Jianchuan basin, are generally flat-lying and partly involved in a broad fold with a NE-trending axis
577 parallel to the striking of the Yulong thrust belt (Fig. 1), which was likely related to the NW-directed
578 compression in a later stage during the basin exhumation at~28-20 Ma (Cao et al., 2019). Therefore,
579 our results indicate a prominent topographic gradient in the hanging wall of the LZF that supplied clasts
580 to the nearby lowland-Jianchuan basin, and thus support a relatively lower surface elevation for the
581 Jianchuan basin in the Late Eocene. Independently, an altitude of 0.5-2.9±0.6 km asl. is suggested for
582 the basin by new stable isotope results integrated with fossil pollen coexistence (Wu et al., 2018). The
583 topographic relief generated by intense crustal shortening within the LZTB created a local vertical
584 vegetation variation (Fig. 8), consistent with the wide range of pollen assemblage and major flood
585 events documented in the Late Eocene sediments of the basin (Sorrel et al., 2017; Wu et al., 2018).
586
587 The collision between Indian and Asian plates since ~60-50 Ma (Allègre et al., 1984; Ding et al., 2016;
588 Hu et al., 2016; Najman et al., 2010; Rowley, 1996) has induced widespread deformation across the
589 Tibetan Plateau, but the details of strain propagation remains debated. Apart from the Himalayan fold-
590 thrust belt bounding the collision belt (Guillot et al., 2003; DeCelles et al., 2014), a growing body of
591 studies documented extensive upper crustal shortening and development of syn-contractional basins
592 within the Qiangtang terrane coevally with or shortly after the onset of the India-Asian collision (Fig.
593 9). For example, geological mapping integrated with balanced cross section and radiometric dating
594 revealed upper crustal shortening of 34±12 km and ~61 km in the Hoh Xil basin and Yushu-Nangqian
595 basin since ~48-52 Ma and ~51 Ma (Horton et al., 2002; Spurlin et al., 2005; Wang et al., 2008; Staisch
596 et al., 2016), respectively. This is also the case for the crustal shortening deformation in the Gonjo basin
597 and LZTB in east and southeast Tibet (Studnicki-Gizbert et al., 2008; Tong et al., 2017; Yin and
598 Harrison, 2000; Gourbet et al., 2017; this study; Fig. 9). In contrast, limited post-50 Ma shortening have
599 been documented in the interiors of the Lhasa, Songpan-Garze and Kunlun terranes (Kapp et al., 2005,
600 2007; van Hinsbergen et al., 2011). Such an intervening deformation pattern implies that the whole
601 Plateau has not been homogenously shortened and thickened in the early stage of the collision as often
602 assumed (Dewey and Burke, 1973; England and Houseman, 1986).
603
604 The deformation pattern approximately fit with the proposition of an Eocene Tibet corresponding to the
605 Qiangtang terrane (Tapponnier et al., 2001). However, other compressional structures, including the

Main Pamir thrust-West Kunlun thrust belt (Cao et al., 2013, 2015; Yin et al., 2002), the Lungmuco fault (Leloup et al., 2012), Altyn Tagh fault and Qaidam thrust (Yin et al., 2002), Northern Qaidam thrust belt (Yin et al., 2008) and West Qinling thrust (Clark et al., 2010; Duvall et al., 2011), located far away (> 400 to 1400 km) from the plate boundary appear active soon after the collision (Fig. 9). This implies that the compressive stresses as a result of the India-Asian collision have been transmitted efficiently across the whole plateau indicating a rigid-plastic rheology, such that an early Cenozoic stage of deformation along the northern boundary of the plateau preceded the migration to the north of the main deformation events in a stepwise manner (Tapponnier et al., 2001). We thus suggest that the deformation pattern is more complex than simple propagation from central to northern Tibet through time as proposed by Tapponnier et al. (2001). Accordingly, a synthesis of middle Eocene tectonic scenario throughout the India-Asian collision zone illustrates that contraction concentrated in the Qiangtang terrane, which intervened the less deformed Lhasa, Songpan-Garze and Kunlun terranes (Fig. 9). The Eocene contractional structures that localized in the Qiangtang terrane were probably inherited from preexisting structures formed during mid-Cretaceous crustal shortening related to the Lhasa-Qiangtang collision (Kapp et al., 2005, 2007), while deformation in the Songpan-Garze and Kunlun terranes was older. The spaced deformation pattern of crustal shortening may be explained by the difference of deeper crustal strength as the deep crust of the Qiangtang terrane is composed of large volume of mélange and flysch that are relatively weaker than the Lhasa, Songpan-Garze and Kunlun terranes (Kapp et al., 2005).

7. Conclusions

An integration of geological mapping and geochronological and thermochronological dating illustrate Early Cenozoic configuration of tectonic deformation, rock exhumation and basin development on the western margin of the South China block (western Yunnan) during the early stage of the India-Asian collision. The Early Cenozoic deformation is expressed by the LZTB, which is a contractional structure which presently outcrop for ~120 km between the Diancang Shan and Xuelong Shan metamorphic belt in western Yunnan. This deformation belt mainly consists of two major SW-dipping brittle thrust faults, named the Ludian-Zhonghejiang fault (LZF) and the Tongdian fault from east to west. Between them, Permo-Triassic strata are involved in a set of short-wavelength, nearly vertical and southwest-vergent tight folds with axes that trend subparallel to the traces of the principal faults. The Paleocene sediments in the Jianchuan basin were deformed by a long-wavelength, vertical broad syncline. Inverse modeling with multiple low temperature thermochronological data, including ZHe, AHe and AFT, from a Triassic pluton in the hanging wall of the LZF reveals two episodes of accelerated cooling during 125-110 Ma and 50-39 Ma. The Cretaceous cooling event was probably ascribed to crustal thickening during the Lhasa and Qiangtang collision. The Eocene rapid exhumation is interpreted to date the activity of the Ludian-Zhonghejiang fold-thrust system. This timing is corroborated by the intrusive relationship between Eocene magmas of ~35-36 Ma and the fold-thrust belt. The Eocene contraction seemingly controlled deposition of alluvial-fan and braided-river sediments of the Baoxiangsi Fm. in the Jianchuan basin, which is supported by paleoflows and provenance analysis. The contractional deformation likely ended at ~39 Ma reflected by significantly decreasing cooling rates in the thermal history and the occurrence of low-lying palustrine and alluvial-lake depositional systems in the basin since then.

At the plateau scale, our results along with geological records of contraction in central, northern and eastern Tibet document Eocene upper crustal shortening localized in the Himalaya, Qiangtang terrane and northern plateau margins (intervened by Lhasa, Songpan-Garze and Kunlun terranes) together with contractional basin development coevally with, or shortly after, the onset of the India-Asian collision, which is inconsistent with a homogenous crustal thickening (Dewey and Burke, 1973; England and Houseman). Moderate crustal shortening affected a large part of Tibet in a spaced way soon after the collision, prior to the main crustal thickening propagated progressively from south to north (Tapponnier et al., 2001). This spaced deformation pattern of crustal shortening illustrates the strain of the India-Asian collision and convergence propagated from the plate boundary within the Asian continent during the Early Cenozoic in a more complex way than what were assumed in the existing geodynamic models.

Acknowledgements

We thank Peter Decelles and Jay Chapman for enlightening discussion. LA-ICP-MS apatite fission-track dating was accomplished by Paul O'Sullivan and Raymond Donelick at Apatite to Zircon, Inc., Viola, Idaho, USA. We are grateful to Peter Reiners and Uttam Chowdhury for help in the (U-Th)/He lab at University of Arizona. This study was funded by the China Geological Survey (No. DD20190811, 1212011121261), the NSF China (Nos. 41672195, 91755213, 41202144, 41302279), the Fundamental Research Funds for the Central Universities, China University of Geosciences (No. G1323511641) and China Scholarship Council (No. 201606415003). This project was supported by the Cai Yuanpei program (grant number 27968UC) of the China Scholarship Council/French Ministry of Education, and the SYSTER (Institut National des Sciences de l'Univers du CNRS) program. We thank one anonymous reviewer, associate editor and Syed Ali Turab for helpful comments that improved the manuscript, as well as chief editor Wenjiao Xiao for editorial handling.

Tables

Table 1. Summary of geochronological and thermochronological results within the LZTB, SE Tibet.

Sample ID	Longitude (°E)	Latitude (°N)	Elevation (m)	Zircon U-Pb age (Ma)	Mean ZHe age (Ma)	Pooled AFT age (Ma)	Mean AHe age (Ma)
CD144	99.5151	27.0599	2595	228 ± 5	121 ± 2	35.8 ± 2.8	-
CD145	99.5034	27.0696	2635	-	108 ± 5	-	35.9 ± 3.2
CD146	99.4895	27.0908	2710	-	-	45.3 ± 3.7	-
CD147	99.4851	27.1013	2789	-	-	41.3 ± 3.4	-
CD148	99.4927	27.1031	2939	-	119 ± 7	38.7 ± 3.2	41.7 ± 2.6
CD149	99.4999	27.0996	2985	235 ± 5	-	44.0 ± 3.5	-
CD316	99.6712	26.5934	3143	34.5 ± 1.3*	-	-	-
CD323	99.6616	26.6113	3060	34.3 ± 1.6*	-	-	-
CD325	99.6420	26.6105	2818	36.0 ± 0.5*	-	-	-
CD327	99.6304	26.6027	2806	234 ±9*	-	-	-
CD330	99.6248	26.6014	2842	36.3 ± 0.8*	-	-	-
CD331	99.6171	26.6010	2876	35.3 ± 1.7*	-	-	-
CD335/ CD435	99.6991	26.5534	2592	35.1 ± 0.5*	-	-	-

Note: * denotes youngest peak ages of plutons in ≤ 10% discordance.

Figures

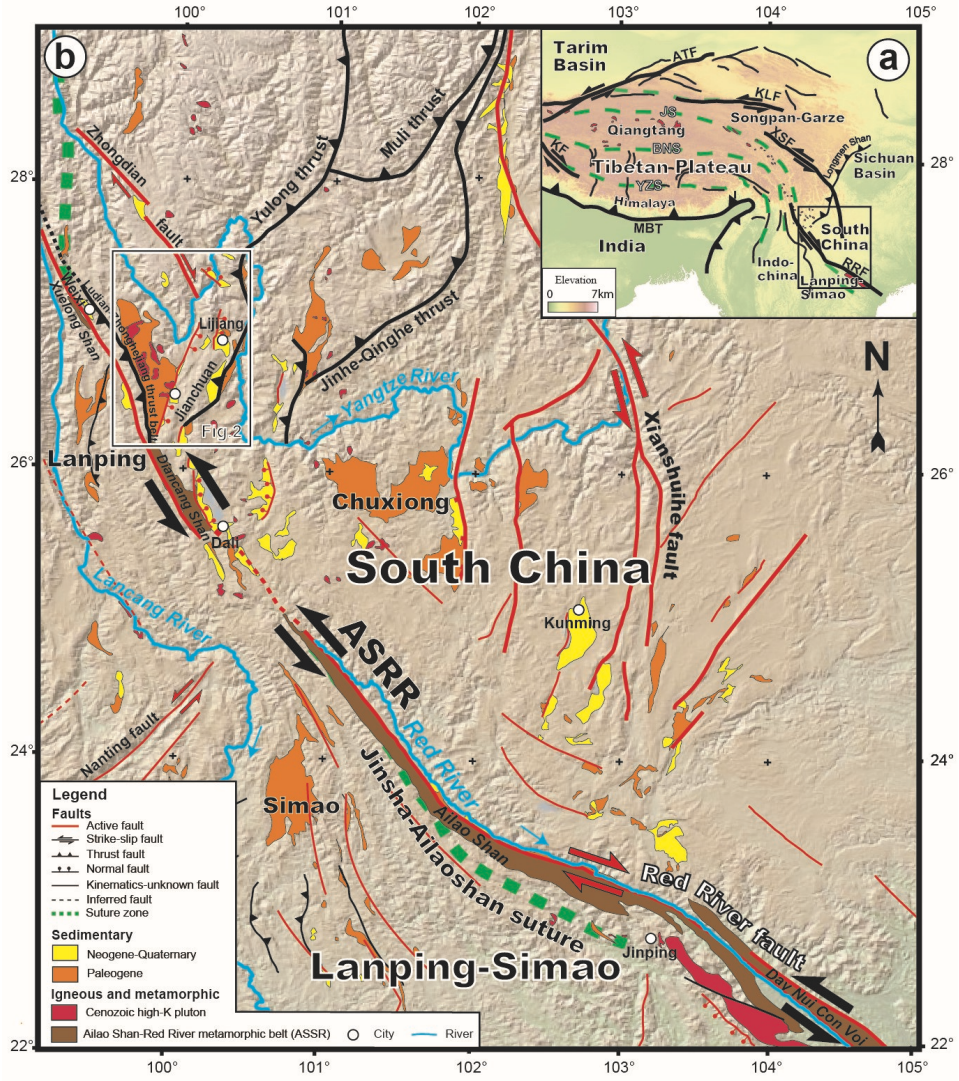

Fig.1 (a) Simplified geological map of the southeast Tibet, showing major Cenozoic structures and basins, modified from Gourbet et al. (2017). Black arrows indicate Oligo-Miocene motion of the ASRR while red arrows indicate Plio-Quaternary motion of the Red River fault. (b) The inset shows location within Tibet. Abbreviations: ATF–Altyn Tagh fault, ASRR–Ailao Shan-Red River shear zone, BNS–Bangong-Nujiang suture, MBT–Main boundary thrust, JS–Jinsha suture, KLF–Kunlun fault, KF–Karakorum fault, RRF–Red River fault, XSF–Xianshuihe fault, IYS–Indus-Yarlung suture.

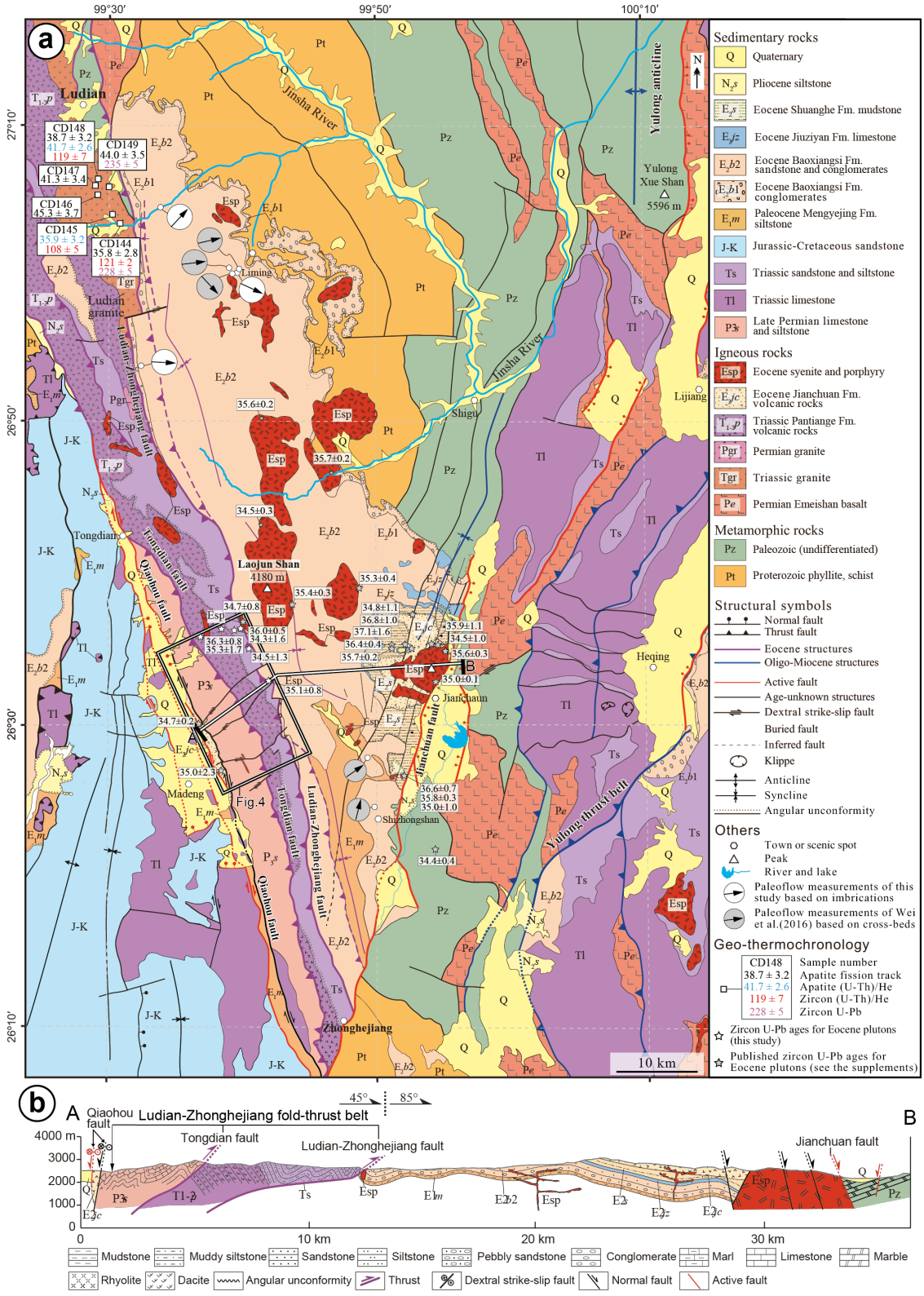

Fig.2 (a) Geological map of the Jianchuan area, southeast Tibet, based on BGMRY (1990), Gourbet et al. (2017), Cao et al. (2019) and new mapping results. See location on Fig. 1a. Geochronology and thermochronology ages are indicated from this study and previous studies in the Tables 1 and S2-S6, as well as paleocurrent directions in the Baoxiangsi Fm. (E_2b) from this study and Wei et al. (2016). The frame corresponds to Fig. 4. (b) Sketch geological cross section across the LZTB and the Jianchuan basin, showing relationships between major structures and lithological units. Sections are located on Fig. 2a.

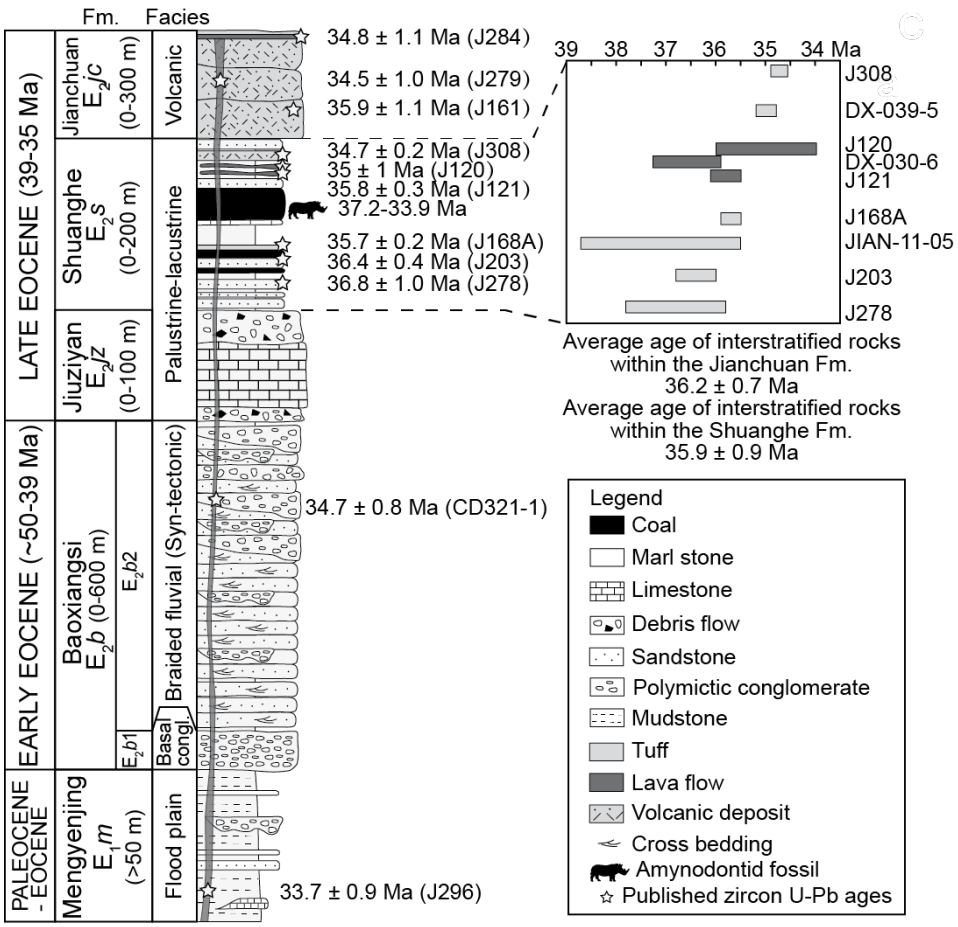

Fig.3 Stratigraphy of the Jianchuan basin with age constraints on the upper part of the sediment sequences, modified from Gourbet et al. (2017) and Sorrel et al. (2017). Age constraints on the sediment sequences are based on Gourbet et al. (2017), Sorrel et al. (2017), Wu et al. (2018) and this study.

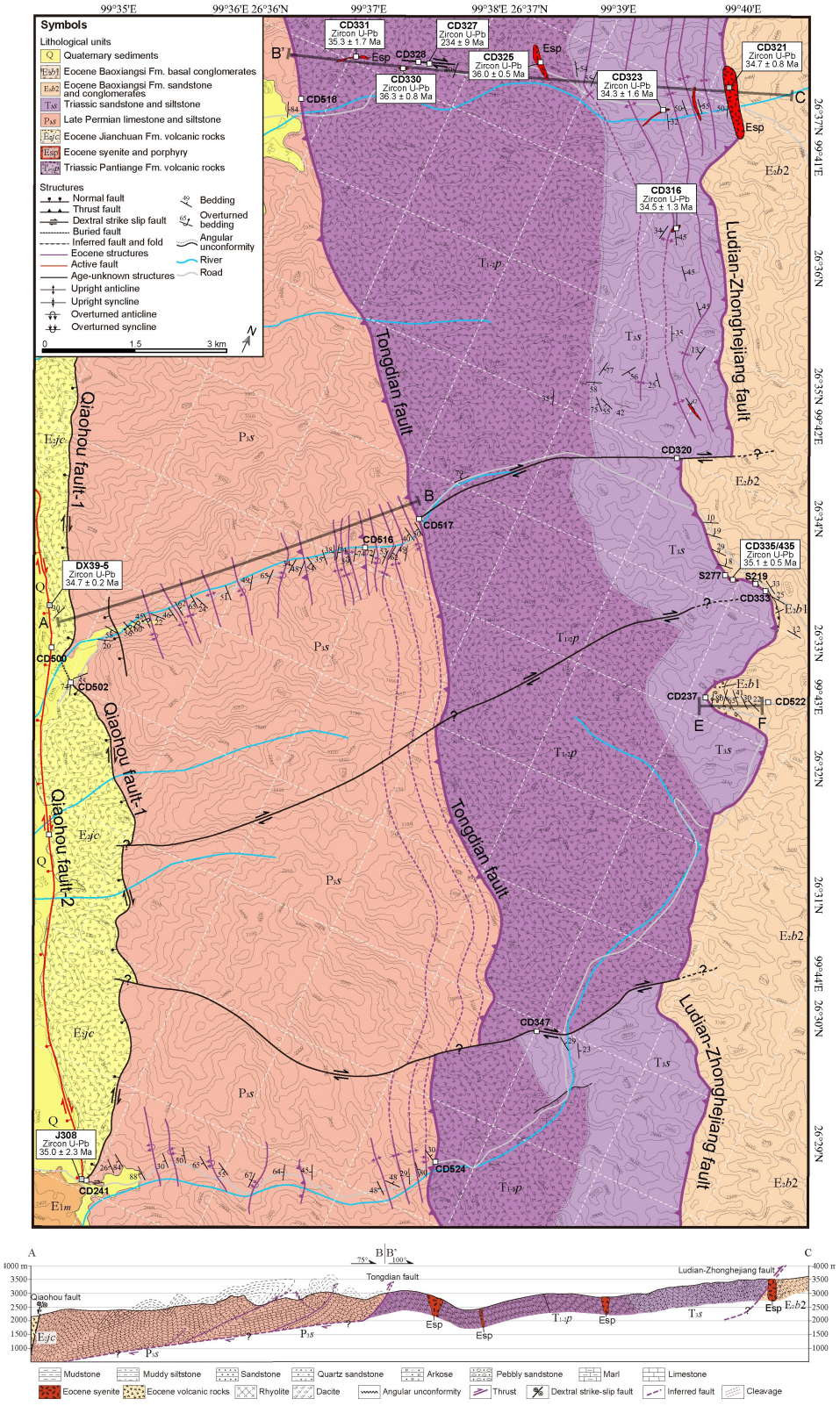

Fig.4 Geological map in the central segment of the LZTB, focusing on the major structures and lithological units to the west of the Jianchuan basin. Mapping based on BGMRY (1990) and this study. The structural measurements for southern section of the mapping area are partly from Tang et al. (2016). Observation sites are shown with corresponding structural observation and samples ages (Table S1). See location on Fig 2a. The lower panel is a composite cross section across the LZTB, composed of A-B, B'-C and E-F segments located on the above panel.

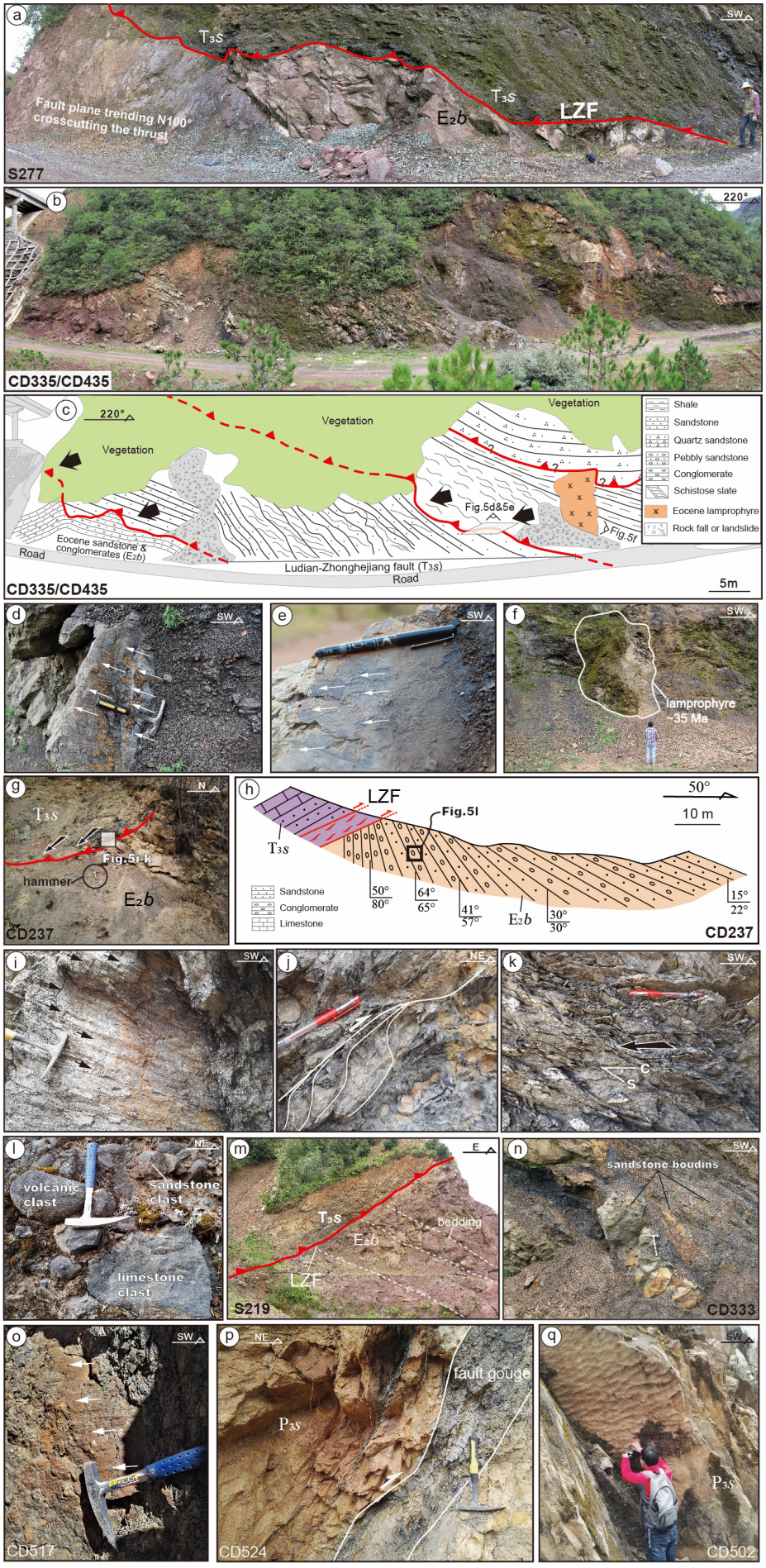
a
SW
T3s
Fault plane trending N100° crosscutting the thrust
T3s
E2b
LZF
S277
b
220°
CD335/CD435
c
220°
Vegetation
Vegetation
Vegetation
Fig.5d&5e
Fig.5f
Eocene sandstone & conglomerates (E2b)
Road
Ludian-Zhonghejiang fault (T3s)
Road
CD335/CD435
5m
Shale
Sandstone
Quartz sandstone
Pebbly sandstone
Conglomerate
Schistose slate
Eocene lamprophyre
Rock fall or landslide
d
SW
e
SW
f
SW
lamprophyre ~35 Ma
g
N
T3s
Fig.5i-k
hammer
E2b
CD237
h
LZF
Fig.5l
50°
10 m
T3s
Sandstone
Conglomerate
Limestone
50° 80°
64° 65°
41° 57°
E2b
30° 30°
15° 22°
CD237
i
SW
j
NE
k
SW
C
S
l
NE
volcanic clast
sandstone clast
limestone clast
m
E
T3s
E2b
bedding
LZF
S219
n
SW
sandstone boudins
CD333
o
SW
CD517
p
NE
fault gouge
P3s
CD524
q
SW
P3s
CD502

Fig.5 Photos showing the main structures of the LZTB. (a) Triassic slate thrusted above Eocene sediments at site S277. (b-f) field observations at site CD335/CD435: (b) field photo and (c) corresponding sketch interpretation, showing schistosed Triassic meta-sandstone and coal-bearing slate (T_3s) resting above folded Eocene sandstones and conglomerates (E_2b1/ E_2b2). Black arrows indicate the direction of motion given by the striae (d-e) gently dipping fault within the Triassic metasandstone and slate (T_3s) with striae indicative of thrust motion towards the northwest to northeast (see Fig. 6b). (f) a ~35 Ma lamprophyre dyke crosscutting schistosed Triassic slate (T_3s) suggestive of initial thrusting prior to ~35 Ma. (g-l) field observations at sites CD237 and CD522 (cross section E-F on Fig. 4). (g) LZF placing Triassic coal-bearing slates (T_3s) on top of Eocene sandstone (E_2b1) at site CD237. (h) a cross section E-F between CD237 and CD522 showing the LZF placing Triassic strata (T_3s) over the Baoxiangsi Fm. (E_2b). (i) gently dipping striae and slickensides and (j-k) sigmoid breccia lenses and S-C fabrics in highly schistosed Triassic slate (T_3s) indicating top to the NE low-angle thrusting. (l) syn-tectonic conglomerates in the footwall of the LZF near site CD237 with abundant cobbles and boulders of volcanic, sandstone and limestone sourced from the hanging wall of the LZF. (m) Triassic clastic sediments (T_3s) thrusted above Eocene sediments (E_2b2) at site S219. (n) sandstone boudins within the LZF at site CD333. (o) striae and slickensides and (p) fault gouge in the Tongdian fault suggesting thrusting at sites CD517 and CD524. (q) asymmetrical ripples in the Late Permian sandstone near site CD506 indicative of overturned bedding dipping to the SW. All sites are shown in Fig. 4 and Table S1b.

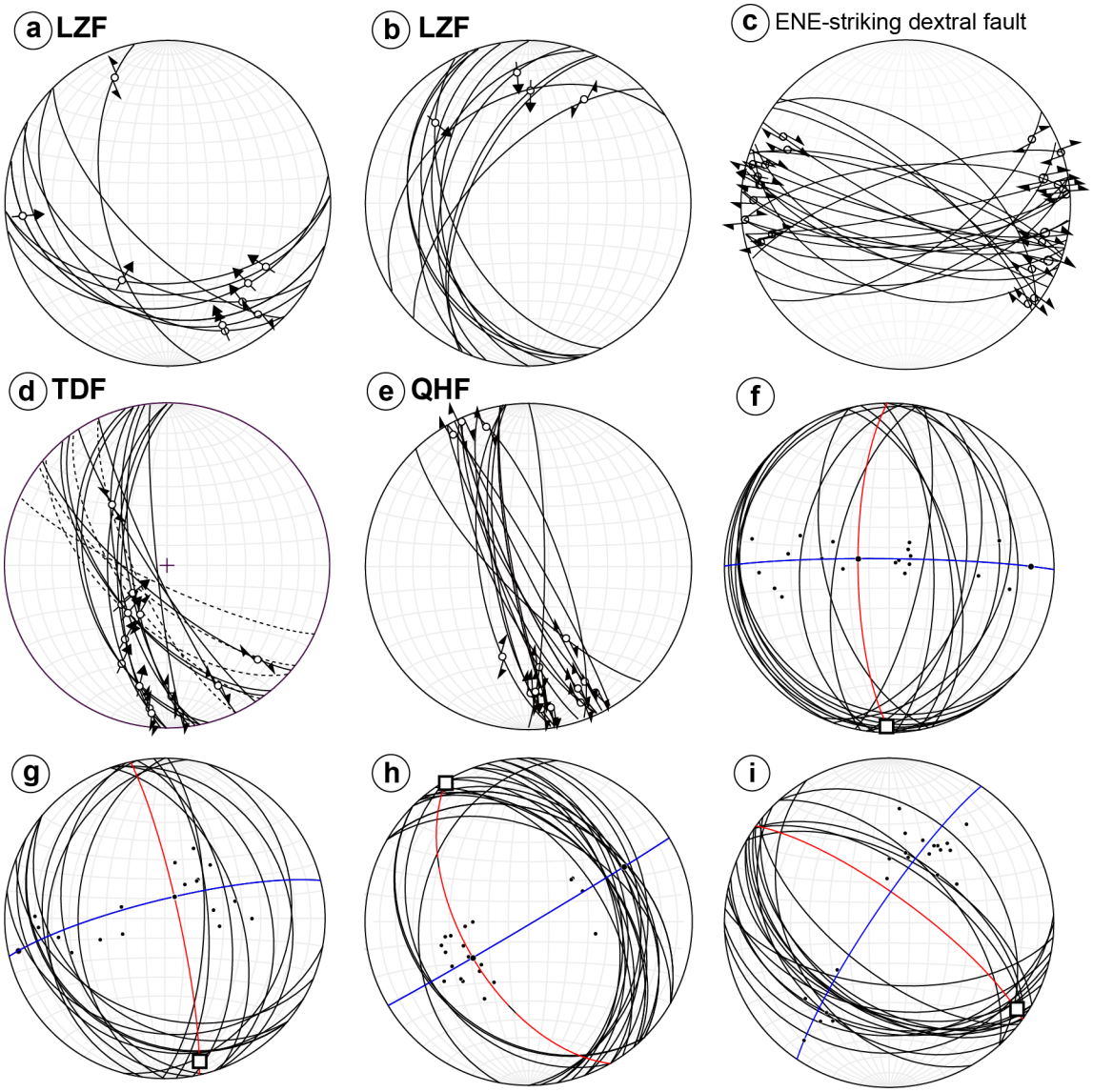

Fig.6 Geometry of faults and folds in the LZTB and western Jianchuan basin. Stereographic projection, lower hemisphere atop the equal area net. (a-b) fault splays within the LZF at outcrops (a) CD335/CD435 and (b) CD237, (c) ENE-striking dextral strike-slip faults at outcrops CD241, CD320, CD327, CD328 and CD347, (d) fault splays (solid curves) within the Tongdian fault (TDF) at outcrops CD516, CD517, CD518 and CD524 and cleavages (dash curves) in the Triassic volcanic rocks close to the TDF at site CD517, (e) fault splays within the Qiaohou fault (QHF) at outcrops CD500 and CD502. Arrows indicate fault kinematics (motion of the upper block). (f-i) stratification (great circles) and poles to stratification (dots). (f) and (g) Eocene sediments (E_2b) in the syncline proximal to the LZF, to the NW and to the SE respectively. (h) and (i) within the fold-thrust belt west of the LZF: Triassic meta-sediments (T_3s) and Late Permian sediments (P_3s) respectively. The axis and hinge orientations of the folds are calculated based on representative strike-and-dip measurements of the limbs of the folded bedding surface. The blue lines are the planes passing by the stratification poles. The red lines are the axial planes with fold axis plotted as squares.

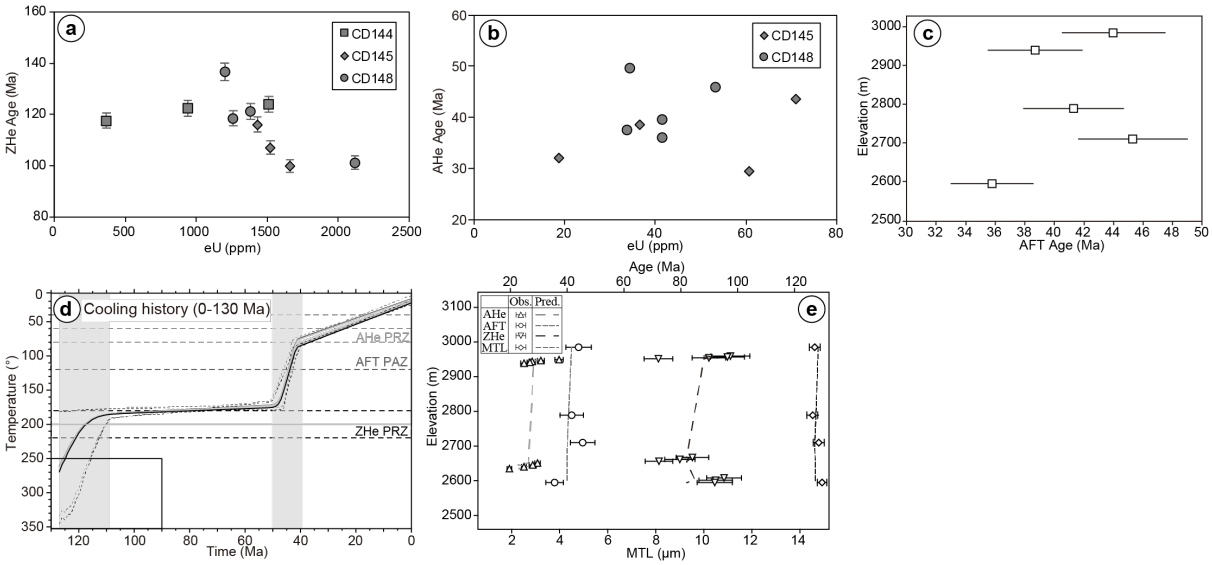

Fig.7 Cooling ages and results of thermal history modelling of the Triassic Ludian granite in the hanging wall of the LZF. (a-b) corrected single-grain ZHe and AHe ages versus effective uranium content (eU). (c) apatite fission-track age and elevation relationship. (d) cooling history of the Ludian granite derived from QTQt inverse modelling with an age-temperature box of 300±50 ℃ and 110±20 Ma as an initial simulation constraint. The thermal history of the uppermost sample is shown in blue, with the 95% confidence interval in cyan, while the thermal history of the lowermost sample is shown in red, with the 95% confidence interval in magenta. Thermal histories for samples at intermediate elevations are in grey. These reflect the combined uncertainty in the inferred thermal history and the offset parameters. (e) the fits of the predicted and observed data.

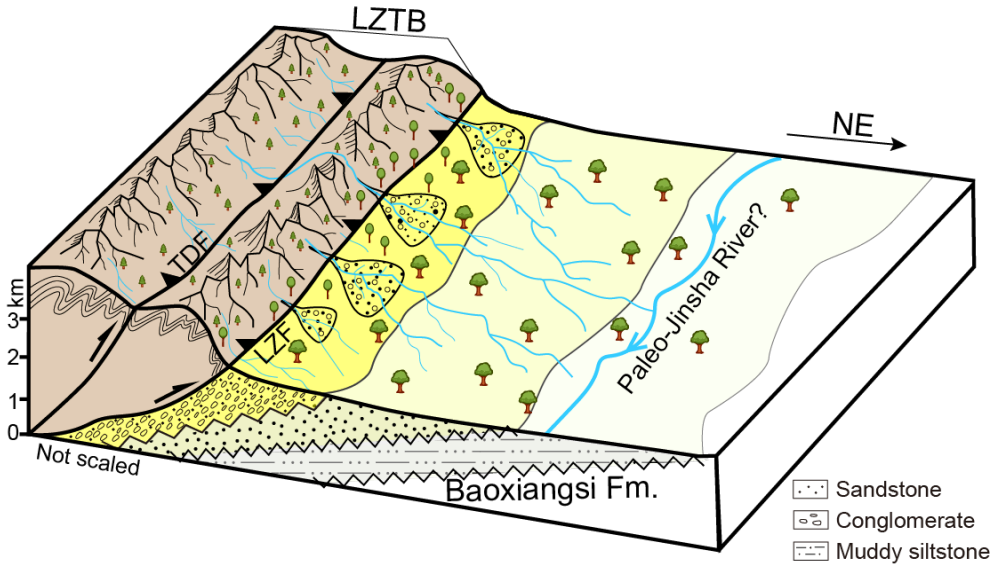

Fig.8 Cartoon showing middle Eocene source-to-sink relationship between the LZTB and syn-tectonic sediments of Baoxiangsi Fm. (E_2b) in the Jianchuan basin. Topographic relief was produced by the activity of the LZTB during ~50-39 Ma, resulting in a high vegetation diversity from the mountains to relatively low-elevation basin recorded by pollen grains (Wu et al., 2018).

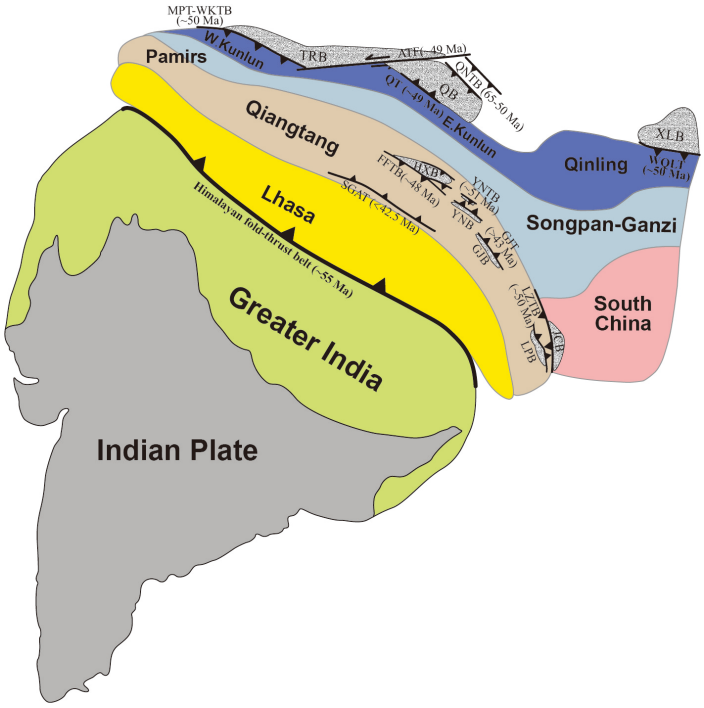

Fig.9 Middle Eocene tectonic scenario across the Tibetan plateau with emphasis on initial activity of the contractional structures and syn-contractional basins immediately after the onset of the India-Asian collision. The size of the Greater India with respect to the Tibet is approximated from van Hinsbergen et al. (2011). Names of the major crustal blocks and sutures are shown. Abbreviations: ATF–Altyn Tagh fault, BNS–Bangong-Nujiang suture, FFTB–Fenghuoshan fold-thrust belt, GJB–Gonjo basin, GJT–Gonjo thrust, HXB–Hoh Xil basin, JCB–Jianchuan basin, JS–Jinsha suture, LMC–Lungmuco fault, LPB–Lanping basin, LZTB–Ludian-Zhonghejiang thrust belt, MPT-WKTB–Main Pamir thrust-West Kunlun thrust belt, QNTB–North Qaidam thrust, YNTB–Yushu-Nangqian thrust belt, YNB–Yushu-Nangqian basin, QB–Qaidam basin, QT–Qaidam thrust, SGAT–Shiquanhe-Gaize-Amdo thrust, TRB–Tarim basin, WQLT–West Qinling thrust, XNB–Xining basin. Initial timing for major faults are labeled: FFTB at ~52-48 Ma (Wang et al., 2008; Staisch et al., 2016); GJT at ~54 Ma (Zhang et al., 2018); Himalayan fold-thrust belt at ~50-45 Ma (Guillot et al., 2003; Decelles et al., 2014); LMC at 60-55 Ma (Leloup et al., 2011); LZTB at 50-39 Ma (this study); MPT-WKTB at ~50 Ma (Cao et al., 2013, 2015; Yin et al., 2002); QNTB at 65-50 Ma (Yin et al., 2008); QT and ATF at ~49 Ma (Yin et al., 2002); SGAT at <42.5 Ma (Yin and Harrison, 2000); WQLT at ~50 Ma (Clark et al., 2010; Duvall et al., 2011), YNTB at ~51 Ma (Horton et al., 2002; Spurlin et al., 2005).

References

Allégre, C. J., Courtillot, V., Tapponnier, P., Hirn, A., Mattauer, M., Coulon, C., Jaeger, J. J., Achache, J., Schärer, U., Marcoux, J., Burg, J. P., Girardeau, J., Armijo, R., Gariépy, C., Göpel, C., Tindong, L., Xuchang, X., Chenfa, C., Guangqin, L., Baoyu, L., Jiwen, T., Naiwen, W., Guoming, C., Tonglin, H., Xibin, W., Wanming, D., Huaibin, S., Yougong, C., Ji, Z., Hongrong, Q., Peisheng, B., Songchan, W., Bixiang, W., Yaoxiu, Z., and Xu, R., 1984, Structure and evolution of the Himalaya–Tibet orogenic belt: Nature, v. 307, no. 5946, p. 17-22.

Allen, C. R., Gillespie, A. R., Han, Y., Sieh, K. E., Zhang, B., and Zhu, C., 1984, Red River and associated faults, Yunnan Province, China: Quaternary geology, slip rates, and seismic hazard: Geological Society of America Bulletin, v. 95, no. 6, p. 686-700.

Bird, P., 1991, Lateral extrusion of lower crust from under high topography in the isostatic limit: Journal of Geophysical Research, v. 96, no. B6, p. 10275-10286.

Burchfiel, B. C., and Chen, Z., 2012, Tectonics of the southeastern Tibetan Plateau and its adjacent foreland: Geological Society of America Memoirs, v. 210, p. 1 -164.

Bureau of Geology and Mineral Resources of Yunnan Province (BGMRY) (1990), Regional Geology of Yunnan Province, 178 pp., Bureau of Geology and Mineral Resources of Yunnan Province, Beijing.

Cao, K., Wang, G., Leloup, P. H., Mahéo, G., Xu, Y., van der Beek, P. A., Replumaz, A., and Zhang, K., 2019, Oligocene-Early Miocene topographic relief generation of southeastern Tibet triggered by thrusting: Tectonics, v. 38, no. 1, p. 374-391.

Cao, K., Wang, G., van der Beek, P., Bernet, M., and Zhang, K., 2013, Cenozoic thermo-tectonic evolution of the northeastern Pamir revealed by zircon and apatite fission-track thermochronology: Tectonophysics, v. 589, p. 17-32.

Cao, K., Wang, G., Bernet, M., van der Beek, P., and Zhang, K., 2015, Exhumation history of the West Kunlun Mountains, northwestern Tibet: Evidence for a long-lived, rejuvenated orogen: Earth and Planetary Science Letters, v. 432, p. 391-403.

Cao, S., Liu, J., Leiss, B., Vollbrecht, A., Genser, J., Neubauer, F., and Zhao, C., 2011, Initiation of left-lateral deformation along the Ailao Shan–Red River shear zone: new microstructural, textural, and geochronological constraints from the Diancang Shan metamorphic massif, SW Yunnan, China: International Geology Review, v. 54, no. 3, p. 348-367.

Cherniak, D. J., Watson, E. B., Grove, M., and Harrison, T. M., 2004, Pb diffusion in monazite: a combined RBS/SIMS study: Geochimica et Cosmochimica Acta, v. 68, no. 4, p. 829-840.

Chung, S., Lee, T., Lo, C., Wang, P., Chen, C., Yem, N. T., Hoa, T. T., and Genyao, W., 1997, Intraplate extension prior to continental extrusion along the Ailao Shan-Red River shear zone: Geology, v. 25, no. 4, p. 311 -314.

Clark, M. K., Farley, K. A., Zheng, D., Wang, Z., and Duvall, A. R., 2010, Early Cenozoic faulting of the northern Tibetan Plateau margin from apatite (U-Th)/He ages: Earth and Planetary Science Letters, v. 296, no. 1-2, p. 78-88.

Clark, M. K., House, M. A., Royden, L. H., Whipple, K. X., Burchfiel, B. C., Zhang, X., and Tang, W., 2005, Late Cenozoic uplift of southeastern Tibet: Geology, v. 33, no. 6, p. 525-528.

Clark, M. K., and Royden, L. H., 2000, Topographic ooze: Building the eastern margin of Tibet by lower crustal flow: Geology, v. 28, no. 8, p. 703-706.

DeCelles, P. G., Robinson, D. M., and Zandt, G., 2002, Implications of shortening in the Himalayan fold-thrust belt for uplift of the Tibetan Plateau: Tectonics, v. 21, no. 6, p. 1062.

Decelles, P. G., Kapp, P., Gehrels, G. E., & Ding, L. (2014). Paleocene-Eocene foreland basin evolution in the Himalaya of southern Tibet and Nepal: Implications for the age of initial India-Asia collision. Tectonics, vol. 33, no. 5, p. 824-849.

Deng, J., Wang, Q., Li, G., Li, C., and Wang, C., 2014a, Tethys tectonic evolution and its bearing on the distribution of important mineral deposits in the Sanjiang region, SW China: Gondwana Research, v. 26, no. 2, p. 419-437.

Deng, J., Wang, Q., Li, G., and Santosh, M., 2014b, Cenozoic tectono-magmatic and metallogenic processes in the Sanjiang region, southwestern China: Earth-Science Reviews, v. 138, p. 268-299.

Dewey, J. F., and Burke, K. C. A., 1973, Tibetan, Variscan, and Precambrian basement reactivation: products of continental collision: The Journal of Geology, v. 8, no. 6, p. 683-692.

Duvall, A. R., Clark, M. K., van der Pluijm, B. A., and Li, C., 2011, Direct dating of Eocene reverse faulting in northeastern Tibet using Ar-dating of fault clays and low-temperature thermochronometry: Earth and Planetary Science Letters, v. 304, no. 3-4, p. 520-526.

Ding, L., Qasim, M., Jadoon, I. A. K., Khan, M. A., Xu, Q., Cai, F., Wang, H., Baral, U., and Yue, Y., 2016, The India-Asia collision in north Pakistan: Insight from the U-Pb detrital zircon provenance of Cenozoic foreland basin: Earth and Planetary Science Letters, v. 455, p. 49-61.
England, P. C., and Houseman, G. A., 1986, Finite strain calculations of continental deformation 2. Comparison with the India-Asia collision zone: Journal of Geophysical Research, v. 91, p. 3664-3676.
Faure, M., Lepvrier, C., Nguyen, V. V., Vu, T. V., Lin, W., and Chen, Z., 2014, The South China block-Indochina collision: Where, when, and how? Journal of Asian Earth Sciences, v. 79, p. 260-274.
Galbraith, R. F., and Green, P. F., 1990, Estimating the component ages in a finite mixture: International Journal of Radiation Applications and Instrumentation. Part D. Nuclear Tracks and Radiation Measurements, v. 17, no. 3, p. 197-206.
Gallagher, K., 2012, Transdimensional inverse thermal history modeling for quantitative thermochronology: Journal of Geophysical Research, v. 117, p. B02408.
Gautheron, C., Tassan-Got, L., Barbarand, J., and Pagel, M., 2009, Effect of alpha-damage annealing on apatite (U–Th)/He thermochronology: Chemical Geology, v. 266, no. 3, p. 157-170.
Gourbet, L., Leloup, P. H., Paquette, J., Sorrel, P., Maheo, G., Wang, G., Yadong, X., Cao, K., Antoine, P., Eymard, I., Liu, W., Lu, H., Replumaz, A., Chevalier, M., Kexin, Z., Jing, W., and Shen, T., 2017, Reappraisal of the Jianchuan Cenozoic basin stratigraphy and its implications on the SE Tibetan plateau evolution: Tectonophysics, v. 700-701, p. 162-179.
Guenthner, W. R., Reiners, P. W., Ketcham, R. A., Nasdala, L., and Giester, G., 2013, Helium diffusion in natural zircon: Radiation damage, anisotropy, and the interpretation of zircon (U-Th)/He thermochronology: American Journal of Science, v. 313, no. 3, p. 145-198.
Guillot, S., Garzanti, E., Baratoux, D., Marquer, D., Mahéo, G., & De Sigoyer, J. (2003). Reconstructing the total shortening history of the NW Himalaya. Geochemistry, Geophysics, Geosystems, vol. 4(7).
Hoke, G. D., Liu-Zeng, J., Hren, M. T., Wissink, G. K., and Garzione, C. N., 2014, Stable isotopes reveal high southeast Tibetan Plateau margin since the Paleogene: Earth and Planetary Science Letters, v. 394, p. 270-278.
Horton, B. K., Yin, A., Spurlin, M. S., Zhou, J., and Wang, J., 2002, Paleocene–Eocene syncontractional sedimentation in narrow, lacustrine-dominated basins of east-central Tibet: Geological Society of America Bulletin, v. 114, no. 7, p. 771 -786.
Hu, X., Garzanti, E., Wang, J., Huang, W., An, W., and Webb, A., 2016, The timing of India-Asia collision onset – Facts, theories, controversies: Earth-Science Reviews, v. 160, p. 264-299.
Jian, P., Liu, D., Kröner, A., Zhang, Q., Wang, Y., Sun, X., and Zhang, W., 2009a, Devonian to Permian plate tectonic cycle of the Paleo-Tethys Orogen in southwest China (I): Geochemistry of ophiolites, arc/back-arc assemblages and within-plate igneous rocks: Lithos, v. 113, no. 3–4, p. 748-766.
Jian, P., Liu, D., Kröner, A., Zhang, Q., Wang, Y., Sun, X., and Zhang, W., 2009b, Devonian to Permian plate tectonic cycle of the Paleo-Tethys Orogen in southwest China (II): Insights from zircon ages of ophiolites, arc/back-arc assemblages and within-plate igneous rocks and generation of the Emeishan CFB province: Lithos, v. 113, no. 3–4, p. 767-784.
Kapp, P., and DeCelles, P. G., 2019, Mesozoic–Cenozoic geological evolution of the Himalayan-Tibetan orogen and working tectonic hypotheses: American Journal of Science, v. 319, no. 3, p. 159 -254.
Kapp, P., DeCelles, P. G., Gehrels, G. E., Heizler, M., and Ding, L., 2007, Geological records of the Lhasa-Qiangtang and Indo-Asian collisions in the Nima area of central Tibet: Geological Society of America Bulletin, v. 119, no. 7-8, p. 917 -933.
Kapp, P., Yin, A., Harrison, T. M., and Ding, L., 2005, Cretaceous-Tertiary shortening, basin development, and volcanism in central Tibet: Geological Society of America Bulletin, v. 117, no. 7-8, p. 865-878.
Ketcham, R. A., Carter, A., Donelick, R. A., Barbarand, J., and Hurford, A. J., 2007, Improved modeling of fission-track annealing in apatite: American Mineralogist, v. 92, no. 5-6, p. 799-810.
Leloup, P. H., Arnaud, N., Lacassin, R., Kienast, J. R., Harrison, T. M., Trong, T. T. P., Replumaz, A., and Tapponnier, P., 2001, New constraints on the structure, thermochronology, and timing of the Ailao Shan-Red River shear zone, SE Asia: Journal of Geophysical Research, v. 106, p. 6683-6732.
Leloup, P. H., Harrison, T. M., Ryerson, F. J., Wenji, C., Qi, L., Tapponnier, P., and Lacassin, R., 1993, Structural, petrological and thermal evolution of a Tertiary ductile strike-slip shear zone, Diancang Shan, Yunnan: Journal of Geophysical Research, v. 98, no. B4, p. 6715-6743.
Leloup, P. H., Lacassin, R., Tapponnier, P., Schärer, U., Zhong, D., Liu, X., Zhang, L., Ji, S., and Trinh, P. T., 1995, The Ailao Shan-Red River shear zone (Yunnan, China), Tertiary transform boundary of Indochina: Tectonophysics, v. 251, no. 1–4, p. 3-84.

888 Leloup, P. H., R. Lacassin, P. Tapponnier; Discussion on the role of the Red River shear zone, Yunnnan and
889 Vietnam, in the continental extrusion of SE Asia; Journal of the geological society, London, vol. 164, p.
890 1253-1260, 2007. DOI: 10.1144/0016-76492007-065
891 Leloup P. H., Arnaud, N.O., Mahéo, G., Paquette, J.L., Guillot, S., Valli, F., Li H., Xu Z., Lacassin, R., and
892 Tapponnier, P, 2012. Successive deformation episodes along the Lungmu Co zone west-central Tibet;
893 Gondwana research, vol. 21, 1, p. 37-52.
894 Li, S., Currie, B. S., Rowley, D. B., and Ingalls, M., 2015, Cenozoic paleoaltimetry of the SE margin of the
895 Tibetan Plateau: Constraints on the tectonic evolution of the region: Earth and Planetary Science Letters,
896 v. 432, p. 415-424.
897 Lin, T., Lo, C., Chung, S., Hsu, F., Yeh, M., Lee, T., Ji, J., Wang, Y., and Liu, D., 2009, $^{40}Ar/^{39}Ar$ dating of
898 the Jiali and Gaoligong shear zones: Implications for crustal deformation around the Eastern Himalayan
899 Syntaxis: Journal of Asian Earth Sciences, v. 34, no. 5, p. 674-685.
900 Liu-Zeng, J., Zhang, J., McPhillips, D., Reiners, P., Wang, W., Pik, R., Zeng, L., Hoke, G., Xie, K., Xiao,
901 P., Zheng, D., and Ge, Y., 2018, Multiple episodes of fast exhumation since Cretaceous in southeast Tibet,
902 revealed by low-temperature thermochronology: Earth and Planetary Science Letters, v. 490, p. 62-76.
903 Metcalfe, I., 2006, Palaeozoic and Mesozoic tectonic evolution and palaeogeography of East Asian crustal
904 fragments: The Korean Peninsula in context: Gondwana Research, v. 9, no. 1, p. 24-46.
905 Meyer, B., Tapponnier, T., Bourjot, L., Métivier, F., Gaudemer, Y., Peltzer, G., Guo, S., and Chen, Z., 1998,
906 Crustal thickening in Gansu-Qinghai, lithospheric mantle subduction, and oblique, strike-slip controlled
907 growth of the Tibet Plateau: Geophysical Journal International, v. 135, no. 1, p. 1-47.
908 Najman, Y., Appel, E., Boudagher-Fadel, M., Bown, P., Carter, A., Garzanti, E., Godin, L., Han, J., Liebke,
909 U., Oliver, G., Parrish, R., and Vezzoli, G., 2010, Timing of India-Asia collision: Geological,
910 biostratigraphic, and palaeomagnetic constraints: Journal of Geophysical Research, v. 115, no. B12, p.
911 B12416.
912 Ouimet, W., Whipple, K., Royden, L., Reiners, P., Hodges, K., and Pringle, M., 2010, Regional incision of
913 the eastern margin of the Tibetan Plateau: Lithosphere, v. 2, no. 1, p. 50-63.
914 Palin, R. M., Searle, M. P., Waters, D. J., Parrish, R. R., Roberts, N. M. W., Horstwood, M. S. A., Yeh, M.
915 W., Chung, S. L., and Anh, T. T., 2013, A geochronological and petrological study of anatectic paragneiss
916 and associated granite dykes from the Day Nui Con Voi metamorphic core complex, North Vietnam:
917 constraints on the timing of metamorphism within the Red River shear zone: Journal of Metamorphic
918 Geology, v. 31, no. 4, p. 359-387.
919 Reiners, P. W., and Brandon, M. T., 2006, Using thermochronology to understand orogenic erosion: Annual
920 Review of Earth and Planetary Sciences, v. 34, p. 419-466.
921 Replumaz, A., Lacassin, R., Tapponnier, P., and Leloup, P. H., 2001, Large river offsets and Plio-Quaternary
922 dextral slip rate on the Red River Fault (Yunnan, China): Journal of Geophysical Research, v. 106, no.
923 B1, p. 819-836.
924 Rowley, D. B., 1996, Age of initiation of collision between India and Asia: A review of stratigraphic data:
925 Earth and Planetary Science Letters, v. 145, no. 1-4, p. 1-13.
926 Royden, L. H., Burchfiel, B. C., King, R. W., Wang, E., Chen, Z., Feng, S., and Liu, Y., 1997, Surface
927 deformation and lower crustal flow in eastern Tibet: Science, v. 276, no. 5313, p. 788-790.
928 Royden, L. H., Burchfiel, B. C., and van der Hilst, R. D., 2008, The Geological Evolution of the Tibetan
929 Plateau: Science, v. 321, no. 5892, p. 1054-1058.
930 Schoenbohm, L. M., Burchfiel, B. C., and Liangzhong, C., 2006, Propagation of surface uplift, lower crustal
931 flow, and Cenozoic tectonics of the southeast margin of the Tibetan Plateau: Geology, v. 34, no. 10, p.
932 813 -816.
933 Searle, M.P., 2006, Role of the Red River Shear zone, Yunnan and Vietnam, in the continental extrusion of
934 SE Asia: Journal of the Geological Society, v. 163, p. 1025-1036, doi: 10.1144/0016-76492005-144.
935 Searle, M. P., Yeh, M., Lin, T., and Chung, S., 2010, Structural constraints on the timing of left-lateral shear
936 along the Red River shear zone in the Ailao Shan and Diancang Shan Ranges, Yunnan, SW China:
937 Geosphere, v. 6, no. 4, p. 316 -338.
938 Sorrel, P., Eymard, I., Leloup, P., Maheo, G., Olivier, N., Sterb, M., Gourbet, L., Wang, G., Jing, W., Lu,
939 H., Li, H., Yadong, X., Zhang, K., Cao, K., Chevalier, M., and Replumaz, A., 2017, Wet tropical climate
940 in SE Tibet during the Late Eocene: Scientific Reports, v. 7, no. 1, p. 7809.
941 Spurlin, M. S., Yin, A., Horton, B. K., Zhou, J., and Wang, J., 2005, Structural evolution of the Yushu-
942 Nangqian region and its relationship to syncollisional igneous activity, east-central Tibet: Geological
943 Society of America Bulletin, v. 117, no. 9-10, p. 1293 -1317.

Staisch, L. M., Niemi, N. A., Clark, M. K., and Chang, H., 2016, Eocene to late Oligocene history of crustal shortening within the Hoh Xil Basin and implications for the uplift history of the northern Tibetan Plateau: Tectonics, v. 35, no. 4, p. 862-895.
Studnicki-Gizbert, C. T., 2006, Deformation, erosion and sedimentation in collisional orogens: case studies from eastern Tibet and southwestern China, Massachusetts Institute of Technology, Dept. of Earth, Atmospheric, and Planetary Sciences, p. 296.
Studnicki-Gizbert, C., Burchfiel, B. C., Li, Z., and Chen, Z., 2008, Early Tertiary Gonjo basin, eastern Tibet: Sedimentary and structural record of the early history of India-Asia collision: Geosphere, v. 4, no. 4, p. 713 -735.
Tang, L., Xue, C., Yang, T., Liang, M., Xiang, K., Liao, C., Jiang, L., and Xin, D., 2016, Late Permian to Early Triassic tectonostratigraphy of Madeng area, northwestern Yunnan, S.W. China: Volcanics zircon U-Pb dating: Acta Petrologica Sinica, no. 8, p. 2535-2554.
Tang, M., Liu-Zeng, J., Hoke, G. D., Xu, Q., Wang, W., Li, Z., Zhang, J., and Wang, W., 2017, Paleoelevation reconstruction of the Paleocene-Eocene Gonjo basin, SE-central Tibet: Tectonophysics, v. 712-713, p. 170-181.
Tapponnier, P., and Molnar, P., 1976, Slip-line field theory and large-scale continental tectonics: Nature, v. 264, no. 5584, p. 319-324.
Tapponnier, P., Peltzer, G., Le Dain, A. Y., Armijo, R., and Cobbold, P., 1982, Propagating extrusion tectonics in Asia: New insights from simple experiments with plasticine: Geology, v. 10, no. 12, p. 611.
Tapponnier, P., Lacassin, R., Leloup, P. H., Schaerer, U., Zhong, D., Wu, H., Liu, X., Ji, S., Zhang, L., and Zhong, J., 1990, The Ailao Shan/Red River metamorphic belt; Tertiary left-lateral shear between Indochina and South China: Nature, v. 343, no. 6257, p. 431-437.
Tapponnier, P., Xu, Z., Roger, F., Meyer, B., Arnaud, N., Wittlinger, G., and Yang, J., 2001, Oblique stepwise rise and growth of the Tibet Plateau: Science, v. 294, no. 5547, p. 1671-1677.
Tong, Y., Yang, Z., Jing, X., Zhao, Y., Li, C., Huang, D., and Zhang, X., 2016, New insights into the Cenozoic lateral extrusion of crustal blocks on the southeastern edge of Tibetan Plateau: Evidence from paleomagnetic results from Paleogene sedimentary strata of the Baoshan Terrane: Tectonics, v. 35, no. 11, p. 2494-2514.
Tong, Y., Yang, Z., Mao, C., Pei, J., Pu, Z., and Xu, Y., 2017, Paleomagnetism of Eocene red-beds in the eastern part of the Qiangtang Terrane and its implications for uplift and southward crustal extrusion in the southeastern edge of the Tibetan Plateau: Earth and Planetary Science Letters, v. 475, p. 1-14.
Turab, S. A., Stüwe, K., Stuart, F. M., Chew, D. M., and Cogné, N., 2017, Tectonics drives rapid exhumation of the western Himalayan syntaxis: Evidence from low- temperature thermochronometry of the Neelum valley region, Pakistan: Lithosphere, v. 9, no. 6, p. 874-888.
van Hinsbergen, D. J. J., Kapp, P., Dupont-Nivet, G., Lippert, P. C., DeCelles, P. G., and Torsvik, T. H., 2011, Restoration of Cenozoic deformation in Asia and the size of Greater India: Tectonics, v. 30, no. 5, p. TC5003.
Wang, C., Zhao, X., Liu, Z., Lippert, P. C., Graham, S. A., Coe, R. S., Yi, H., Zhu, L., Liu, S., and Li, Y., 2008, Constraints on the early uplift history of the Tibetan Plateau: Proceedings of the National Academy of Sciences, v. 105, no. 13, p. 4987-4992.
Wang, E., Burchfiel, B. C., Royden, L. H., Chen, L., Chen, J., Li, W., and Chen, Z., 1998, Late Cenozoic Xianshuihe-Xiaojiang, Red River, and Dali Fault Systems of Southwestern Sichuan and Central Yunnan, China: Geological Society of America Special Papers, v. 327, p. 1 -108.
Wang, J., Yin, A., Harrison, T. M., Grove, M., Zhang, Y., and Xie, G., 2001, A tectonic model for Cenozoic igneous activities in the eastern Indo–Asian collision zone: Earth and Planetary Science Letters, v. 188, no. 1–2, p. 123-133.
Wang, Y., Zhang, B., Schoenbohm, L. M., Zhang, J., Zhou, R., Hou, J., and Ai, S., 2016, Late Cenozoic tectonic evolution of the Ailao Shan-Red River fault (SE Tibet): Implications for kinematic change during plateau growth: Tectonics, v. 35, no. 8, p. 1969-1988.
Wei, H., Wang, E., Wu, G., and Meng, K., 2016, No sedimentary records indicating southerly flow of the paleo-Upper Yangtze River from the First Bend in southeastern Tibet: Gondwana Research, v. 32, p. 93-104.
Wissink, G. K., Hoke, G. D., Garzione, C. N., and Liu-Zeng, J., 2016, Temporal and spatial patterns of sediment routing across the southeast margin of the Tibetan Plateau: Insights from detrital zircon: Tectonics, v. 35, no. 11, p. 2538-2563.

Wu, J., Zhang, K., Xu, Y., Wang, G., Garzione, C. N., Eiler, J., Leloup, P. H., Sorrel, P., and Mahéo, G., 2018, Paleoelevations in the Jianchuan Basin of the southeastern Tibetan Plateau based on stable isotope and pollen grain analyses: Palaeogeography, Palaeoclimatology, Palaeoecology, v. 510, p. 93-108.

Yang, T. N., Liang, M. J., Fan, J. W., Shi, P. L., Zhang, H. R., and Hou, Z. H., 2014, Paleogene sedimentation, volcanism, and deformation in eastern Tibet: Evidence from structures, geochemistry, and zircon U–Pb dating in the Jianchuan Basin, SW China: Gondwana Research, v. 26, no. 2, p. 521-535.

Yin, A., 2010, Cenozoic tectonic evolution of Asia: A preliminary synthesis: Tectonophysics, v. 488, no. 1, p. 293-325.

Yin, A., Dang, Y., Wang, L., Jiang, W., Zhou, S., Chen, X., Gehrels, G. E., and McRivette, M. W., 2008, Cenozoic tectonic evolution of Qaidam basin and its surrounding regions (Part 1): The southern Qilian Shan-Nan Shan thrust belt and northern Qaidam basin: Geological Society of America Bulletin, v. 120, no. 7-8, p. 813-846.

Yin, A., Rumelhart, P. E., Butler, R., Cowgill, E., Harrison, T. M., Foster, D. A., Ingersoll, R. V., Qing, Z., Xian-Qiang, Z., Xiao-Feng, W., Hanson, A., and Raza, A., 2002, Tectonic history of the Altyn Tagh fault system in northern Tibet inferred from Cenozoic sedimentation: Geological Society of America Bulletin, v. 114, no. 10, p. 1257-1295.

Yin, A., and Harrison, T. M., 2000, Geologic Evolution of the Himalayan-Tibetan Orogen: Annual Review of Earth and Planetary Sciences, v. 28, no. 1, p. 211-280.

Zhang, B., Zhang, J., Liu, J., Wang, Y., Yin, C., Guo, L., Zhong, D., Lai, Q., and Yue, Y., 2014, The Xuelongshan high strain zone: Cenozoic structural evolution and implications for fault linkages and deformation along the Ailao Shan–Red River shear zone: Journal of Structural Geology, v. 69, p. 209-233.

Zhang, B., Zhang, J., Zhong, D., Wang, X., Qu, J., and Guo, L., 2011, Structural feature and its significance of the northernmost segment of the Tertiary Biluoxueshan-Chongshan shear zone, east of the Eastern Himalayan Syntaxis: Science China Earth Sciences, v. 54, no. 7, p. 959-974.

Zhang, B., Zhang, J., and Zhong, D., 2010, Structure, kinematics and ages of transpression during strain-partitioning in the Chongshan shear zone, western Yunnan, China: Journal of Structural Geology, v. 32, no. 4, p. 445-463.

Zhang, Y., Huang, W., Huang, B., van Hinsbergen, D. J. J., Yang, T., Dupont-Nivet, G., and Guo, Z., 2018, 53-43 Ma deformation of eastern Tibet revealed by three stages of tectonic rotation in the Gongjue Basin: Journal of Geophysical Research: Solid Earth, v. 123, no. 5, p. 3320-3338.

Zhang, Y., Replumaz, A., Leloup, P. H., Wang, G., Bernet, M., van der Beek, P., Paquette, J. L., and Chevalier, M., 2017, Cooling history of the Gongga batholith: Implications for the Xianshuihe Fault and Miocene kinematics of SE Tibet: Earth and Planetary Science Letters, v. 465, p. 1-15.

Zhang, Y., Replumaz, A., Wang, G., Leloup, P. H., Gautheron, C., Bernet, M., Beek, P., Paquette, J. L., Wang, A., Zhang, K., Chevalier, M., and Li, H., 2015, Timing and rate of exhumation along the Litang fault system, implication for fault reorganization in Southeast Tibet: Tectonics, v. 34, no. 6, p. 1219-1243.

Zi, J., Cawood, P. A., Fan, W., Tohver, E., Wang, Y., McCuaig, T. C., and Peng, T., 2013, Late Permian-Triassic magmatic evolution in the Jinshajiang orogenic belt, SW China and implications for orogenic processes following closure of the Paleo-Tethys: American Journal of Science, v. 313, no. 2, p. 81 -112.

Zi, J., Cawood, P. A., Fan, W., Tohver, E., Wang, Y., and McCuaig, T. C., 2012, Generation of Early Indosinian enriched mantle-derived granitoid pluton in the Sanjiang Orogen (SW China) in response to closure of the Paleo-Tethys: Lithos, v. 140-141, p. 166-182.

Appendix

Supplementary material S1 Analytical procedures for geochronology and thermochronology

Zircon U-Pb geochronology

Zircon U-Pb geochronological analyses were conducted at China University of Geosciences, Wuhan, China. U-Pb dating was performed using an Agilent 7500a ICP-MS, which is equipped with a GeoLas 2005 excimer laser ablation system at a spot diameter of 32 μm. Zircon 91500 was used as an external standard and analyzed twice every 5 unknowns. To keep age reproducibility and instrument stability, four GJ-1 zircon standards were inserted at the beginning and end of each run. Typical operating conditions and detailed analytical procedures are described in (Liu et al., 2008). Selection and integration of analytic signals, time-drift correction, and quantitative calibration for U-Pb dating were performed by ICP-MS DataCal. Ages were accepted with up to 10% and 20% discordance for plutonic and volcanic samples, respectively. The results reported here are $^{206}Pb/^{238}U$ ages for zircon ages ≤1.0 Ga and $^{207}Pb/^{206}Pb$ ages for grains with ages >1.0 Ga. Age-distribution plots and age-concordia diagrams were generated using Isoplot/Ex. ver. 3.75 (Ludwig, 2012).

Low-temperature thermochronology

Apatite fission track analysis was performed at Apatite to Zircon, Inc., Viola, Idaho, USA. Apatite aliquots were mounted in epoxy and polished, and then etched in a 5.5 M HNO_3 solution at 21°C for 20 s. Apatite fission track data were acquired using a New Wave Neodymium-YAG 213 nm laser ablation system coupled to a Finigan Element II Magnetic Sector ICP-MS at a 12 μm spot and a 5 Hz repetition rate with the laser set in constant energy mode. Analyses were corrected by ^{43}Ca as an internal standard for variations in ablation volume. For detailed procedures of sample analysis refer to Donelick et al. (2005)

Zircon and Apatite (U-Th)/He dating was accomplished at the University of Arizona, USA. Normally, 3-5 euhedral zircon and apatite crystals without visible inclusions, fracture and stainless surface were chosen using a stereo-zoom polarized microscope. The geometry of each grain was measured and photographed. The grains larger than 60 μm but smaller than 500 μm in both length and width were accepted to processed for (U-Th)/He analysis. The zircon and apatite grains were wrapped into Nb foil tubes and degassed by laser heating, and then analyzed for He using ^{3}He isotope dilution, cryogenic purification and quadrupole mass spectrometry. The U, Th and Sm concentrations of each dissolved aliquots was measured on a sector inductively coupled plasma-mass spectrometer. Corrected (U-Th)/He ages were processed by applying the α-ejection correction factor (Farley, 2002). Standard Fish Canyon Tuff zircon and Durango apatite fragments were identically analyzed together with unknowns to validate age determination, age reproducibility and measurement accuracy. Mean ages of each sample were calculated based on all grain ages and relevant errors.

References

Donelick, R. A., O'Sullivan, P. B., and Ketcham, R. A., 2005, Apatite Fission-Track Analysis: Reviews in Mineralogy and Geochemistry, v. 58, no. 1, p. 49-94.

Farley, K. A., 2002, (U-Th)/He Dating: Techniques, Calibrations, and Applications: Reviews in Mineralogy and Geochemistry, v. 47, no. 1, p. 819-844.

Liu, Y., Hu, Z., Gao, S., Günther, D., Xu, J., Gao, C., and Chen, H., 2008, In situ analysis of major and trace elements of anhydrous minerals by LA-ICP-MS without applying an internal standard: Chemical Geology, v. 257, no. 1–2, p. 34-43.

Ludwig, K. R., 2012, User's Manual for Isoplot 3.75: A geochronological toolkit for microsoft excel: Berkeley, California, Berkeley Geochronology Center Special Publication No. 5, 1-75 p.

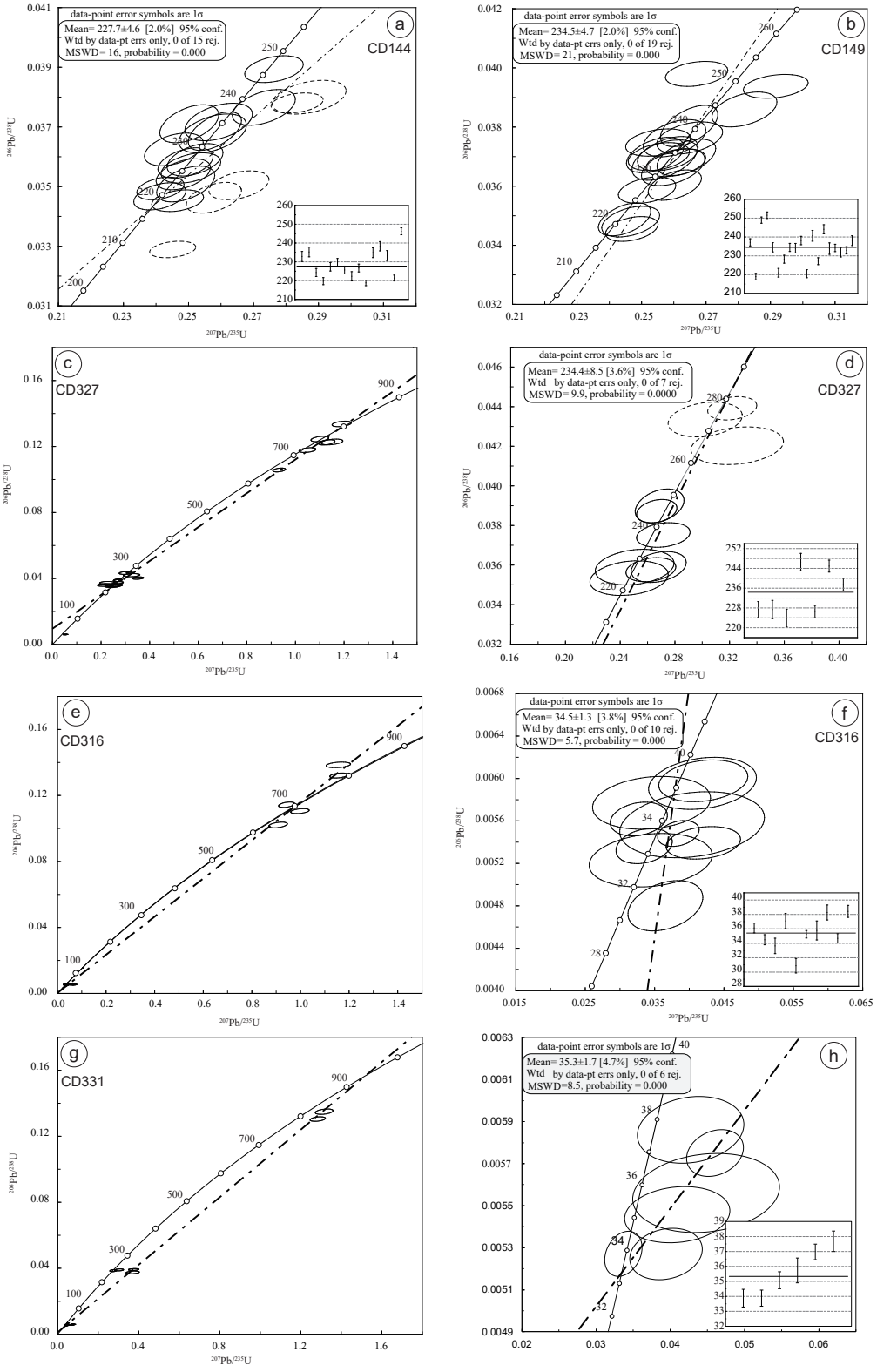

Fig. S1 Concordia diagrams and weighted mean ages of zircon U-Pb samples. The ages that were not used for final age calculation were marked by dashed ellipses on concordia diagram.

1096

Table S1a Sample location and description.

Location	Sample ID	Lithology	Era	Longitude (°E)	Latitude (°N)	Elevation (m)
Weixi	CD144	Granite	Triassic	99.5151	27.0599	2595
Weixi	CD145	Granite	Triassic	99.5034	27.0696	2635
Weixi	CD146	Granite	Triassic	99.4895	27.0908	2710
Weixi	CD147	Granite	Triassic	99.4851	27.1013	2789
Weixi	CD148	Granite	Triassic	99.4927	27.1031	2939
Weixi	CD149	Granite	Triassic	99.4999	27.0996	2985
Laojun Shan	CD316	Porphyry	Eocene	99.6712	26.5934	3143
Laojun Shan	CD323	Granitic porphyry	Eocene	99.6616	26.6113	3060
Laojun Shan	CD325	Granite	Eocene	99.6420	26.6105	2818
Laojun Shan	CD327	Dacite	Triassic	99.6304	26.6027	2806
Laojun Shan	CD330	Granitic porphyry	Eocene	99.6248	26.6014	2842
Laojun Shan	CD331	Granitic porphyry	Eocene	99.6171	26.6010	2876
Laojun Shan	CD335	Lamprophyre	Eocene	99.6991	26.5534	2592
Laojun Shan	CD435	Lamprophyre	Eocene	99.6991	26.5534	2592

1097

Table S1b Sites for structural and sedimentary observations.

Sites	Longitude (°E)	Latitude (°N)	Target
CD237	99.7031	26.5370	Ludian-Zhonghejiang fault
S219	99.7030	26.5534	Ludian-Zhonghejiang fault
S277	99.6942	26.5545	Ludian-Zhonghejiang fault
CD333	99.7057	26.5532	Ludian-Zhonghejiang fault
CD335/CD435	99.6991	26.5534	Ludian-Zhonghejiang fault
CD320	99.6851	26.5668	ENE-trending dextral fault
CD327	99.6304	26.6027	ENE-trending dextral fault
CD328	99.6267	26.6023	ENE-trending dextral fault
CD347	99.7060	26.4792	ENE-trending dextral fault
CD241	99.6479	26.4346	Qiaohou fault and ENE-trending dextral fault
CD502	99.6168	26.5003	Qiaohou fault
CD517	99.6556	26.5408	Tongdian fault
CD518	99.6136	26.5903	Tongdian fault
CD524	99.6943	26.4586	Tongdian fault
CD522	99.7081	26.5396	Baoxiangsi Formation

Table S2 Zircon U-Pb geochronologic data analyzed by Laser-Ablation ICP Mass Spectrometry.

				Isotopic ratios					Apparent ages (Ma)							
Sample #	U	Th	U/Th	207Pb*	±	206Pb*	±	error	206Pb*	±	207Pb*	±	207Pb*	±	Best age	±	
Analysis	(ppm)	(ppm)		235U	(%)	238U	(%)	corr.	238U	(Ma)	235U	(Ma)	206Pb*	(Ma)	(Ma)	(Ma)	Discordance
CD144																	
CD144-1-1	7136	2201	3.2	0.2578	0.0056	0.0346	0.0003	0.4525	219.4	2.1	232.9	4.5	372.3	50.0	219.4	2.1	6%
CD144-1-2	5259	1320	4.0	0.2574	0.0069	0.0368	0.0004	0.4389	232.8	2.7	232.6	5.5	227.8	57.4	232.8	2.7	0%
CD144-1-3	4757	1230	3.9	0.2593	0.0068	0.0372	0.0004	0.4218	235.2	2.6	234.1	5.5	213.0	55.5	235.2	2.6	0%
CD144-1-4	6075	1640	3.7	0.2484	0.0055	0.0354	0.0003	0.4362	224.3	2.1	225.3	4.5	227.8	43.5	224.3	2.1	0%
CD144-1-5	6939	1356	5.1	0.2412	0.0053	0.0347	0.0003	0.3948	219.7	1.9	219.4	4.3	213.0	50.0	219.7	1.9	0%
CD144-1-6	5746	1814	3.2	0.2520	0.0057	0.0359	0.0004	0.4433	227.4	2.2	228.2	4.6	235.3	50.0	227.4	2.2	0%
CD144-1-7	5197	1154	4.5	0.2455	0.0060	0.0362	0.0004	0.4112	229.5	2.3	222.9	4.9	142.7	47.2	229.5	2.3	3%
CD144-1-8	5135	1528	3.4	0.2508	0.0060	0.0356	0.0003	0.3900	225.7	2.1	227.2	4.9	231.6	47.2	225.7	2.1	1%
CD144-1-9	5066	967	5.2	0.2491	0.0059	0.0351	0.0004	0.4766	222.3	2.5	225.9	4.8	261.2	56.5	222.3	2.5	2%
CD144-1-10	7971	1840	4.3	0.2452	0.0047	0.0329	0.0002	0.2864	208.6	1.1	222.6	3.8	361.2	73.1	208.6	1.1	6%
CD144-1-11	5171	1664	3.1	0.2871	0.0075	0.0380	0.0004	0.3801	240.4	2.3	256.3	5.9	390.8	49.1	240.4	2.3	6%
CD144-1-12	5909	1839	3.2	0.2491	0.0056	0.0358	0.0003	0.4163	226.7	2.1	225.8	4.5	213.0	50.0	226.7	2.1	0%
CD144-1-13	6337	1324	4.8	0.2467	0.0053	0.0345	0.0002	0.3264	218.8	1.5	223.9	4.3	272.3	43.5	218.8	1.5	2%
CD144-1-14	5490	1908	2.9	0.2835	0.0053	0.0378	0.0002	0.3118	239.2	1.4	253.4	4.2	383.4	47.2	239.2	1.4	6%
CD144-1-15	5032	796	6.3	0.2502	0.0060	0.0371	0.0004	0.4743	234.9	2.6	226.8	4.9	146.4	49.1	234.9	2.6	4%
CD144-1-16	5235	1506	3.5	0.2732	0.0064	0.0377	0.0004	0.4482	238.3	2.5	245.2	5.1	305.6	50.0	238.3	2.5	3%
CD144-1-17	5291	1234	4.3	0.2581	0.0054	0.0369	0.0004	0.5534	233.3	2.7	233.2	4.4	235.3	48.1	233.3	2.7	0%
CD144-1-18	7296	2040	3.6	0.2414	0.0048	0.0349	0.0003	0.3612	221.4	1.6	219.5	3.9	194.5	46.3	221.4	1.6	1%
CD144-1-19	5257	1132	4.6	0.2763	0.0059	0.0389	0.0003	0.3539	246.2	1.8	247.7	4.7	253.8	46.3	246.2	1.8	1%
CD144-1-20	6596	1513	4.4	0.2655	0.0061	0.0350	0.0003	0.3964	222.0	2.0	239.1	4.9	466.7	48.1	222.0	2.0	7%
CD149																	
CD149-2-1	5020	1382	3.6	0.2551	0.0066	0.0375	0.0003	0.3126	237.2	1.9	230.7	5.4	161.2	57.4	237.2	1.9	3%
CD149-2-2	6844	1788	3.8	0.2470	0.0054	0.0346	0.0003	0.3682	219.0	1.7	224.1	4.4	276.0	43.5	219.0	1.7	2%
CD149-2-3	4000	1186	3.4	0.2916	0.0066	0.0394	0.0003	0.2970	249.0	1.6	259.8	5.2	366.7	51.8	249.0	1.6	4%
CD149-2-4	3269	805	4.1	0.2671	0.0064	0.0398	0.0003	0.2932	251.6	1.7	240.4	5.1	200.1	57.4	251.6	1.7	5%
CD149-2-5	5276	1058	5.0	0.2542	0.0059	0.0371	0.0004	0.4614	234.5	2.5	230.0	4.7	189.0	50.0	234.5	2.5	2%
CD149-2-6	5795	1075	5.4	0.2447	0.0054	0.0349	0.0004	0.4824	221.0	2.3	222.3	4.4	231.6	46.3	221.0	2.3	1%
CD149-2-7	5110	1023	5.0	0.2603	0.0055	0.0360	0.0003	0.4494	228.2	2.1	234.9	4.4	301.9	48.1	228.2	2.1	3%
CD149-2-8	4607	1195	3.9	0.2581	0.0062	0.0370	0.0003	0.3892	234.5	2.1	233.1	5.0	213.0	51.8	234.5	2.1	1%
CD149-2-9	4747	1412	3.4	0.2639	0.0060	0.0370	0.0004	0.4836	234.1	2.5	237.8	4.8	333.4	48.1	234.1	2.5	2%
CD149-2-10	4069	1256	3.2	0.2649	0.0067	0.0376	0.0004	0.3739	238.1	2.2	238.6	5.4	239.0	55.5	238.1	2.2	0%
CD149-2-11	4731	1399	3.4	0.2466	0.0059	0.0348	0.0003	0.4084	220.5	2.1	223.8	4.8	261.2	55.5	220.5	2.1	1%
CD149-2-12	6056	1851	3.3	0.2648	0.0059	0.0380	0.0005	0.5466	240.6	2.9	238.5	4.7	213.0	44.4	240.6	2.9	1%
CD149-2-13	5837	1262	4.6	0.2517	0.0059	0.0359	0.0003	0.3509	227.1	1.8	228.0	4.8	231.6	47.2	227.1	1.8	0%
CD149-2-14	4177	1186	3.5	0.2819	0.0067	0.0386	0.0004	0.4279	244.1	2.4	252.2	5.3	324.1	50.0	244.1	2.4	3%
CD149-2-15	4738	833	5.7	0.2573	0.0068	0.0369	0.0005	0.5037	233.8	3.0	232.5	5.5	216.7	55.5	233.8	3.0	1%
CD149-2-16	3731	977	3.8	0.2554	0.0063	0.0370	0.0003	0.3441	234.2	1.9	230.9	5.1	211.2	57.4	234.2	1.9	1%
CD149-2-17	5222	1694	3.1	0.2598	0.0065	0.0366	0.0004	0.4481	231.9	2.5	234.5	5.2	253.8	45.4	231.9	2.5	1%
CD149-2-18	6445	1527	4.2	0.2607	0.0061	0.0368	0.0003	0.3607	232.9	1.9	235.2	4.9	253.8	47.2	232.9	1.9	1%
CD149-2-19	4645	1416	3.3	0.2602	0.0064	0.0376	0.0004	0.4502	238.1	2.6	234.8	5.2	211.2	55.5	238.1	2.6	1%
CD149-2-20	5398	1064	5.1	0.3621	0.0115	0.0400	0.0003	0.2637	252.8	2.1	313.7	8.6	772.2	52.8	252.8	2.1	19%
CD316																	
CD316-1-1	558	387	1.4	0.0624	0.0059	0.0056	0.0002	0.3625	35.8	1.2	61.5	5.6	1636.7	244.4	35.8	1.2	42%
CD316-1-2	871	893	1.0	0.0460	0.0044	0.0057	0.0001	0.2569	36.8	0.9	45.7	4.3	738.9	222.2	36.8	0.9	19%
CD316-1-3	577	394	1.5	0.0366	0.0036	0.0048	0.0002	0.3339	30.9	1.0	36.5	3.5	683.3	245.2	30.9	1.0	15%

CD316-1-4	2191	136	16.1	1.1579	0.0244	0.1321	0.0010	0.3603	799.8	5.7	781.0	11.5	722.2	43.7	799.8	5.7	2%
CD316-1-5	442	232	1.9	0.0404	0.0069	0.0056	0.0002	0.2166	35.8	1.3	40.2	6.7	990.7	415.6	35.8	1.3	11%
CD316-1-6	858	325	2.6	0.9079	0.0251	0.1021	0.0011	0.4054	626.8	6.7	655.9	13.4	750.0	61.1	626.8	6.7	4%
CD316-1-7	1548	224	6.9	0.9978	0.0250	0.1105	0.0010	0.3567	675.7	5.7	702.7	12.7	775.9	54.5	675.7	5.7	4%
CD316-1-8	3402	7003	0.5	0.0384	0.0020	0.0055	0.0001	0.2861	35.2	0.5	38.3	1.9	279.7	131.5	35.2	0.5	8%
CD316-1-9	1903	331	5.7	0.9431	0.0216	0.1144	0.0011	0.4151	698.2	6.3	674.5	11.3	583.4	50.0	698.2	6.3	4%
CD316-1-10	472	303	1.6	0.0590	0.0082	0.0054	0.0002	0.2254	34.7	1.1	58.2	7.8	1418.2	289.4	34.7	1.1	40%
CD316-1-11	535	362	1.5	0.0344	0.0059	0.0052	0.0002	0.1872	33.6	1.1	34.4	5.7	305.6	322.2	33.6	1.1	2%
CD316-1-12	1382	1523	0.9	0.0335	0.0027	0.0054	0.0001	0.2550	34.5	0.7	33.4	2.6	100.1	179.6	34.5	0.7	3%
CD316-1-13	559	388	1.4	0.0653	0.0064	0.0058	0.0002	0.3606	37.1	1.3	64.2	6.1	1457.4	201.9	37.1	1.3	42%
CD316-1-14	556	436	1.3	0.0695	0.0061	0.0053	0.0002	0.3520	34.3	1.1	68.2	5.8	1820.7	197.4	34.3	1.1	50%
CD316-1-15	1369	344	4.0	1.1559	0.0330	0.1385	0.0011	0.2848	836.4	6.4	780.0	15.6	633.4	61.1	836.4	6.4	7%
CD316-1-16	1127	821	1.4	0.0420	0.0042	0.0060	0.0001	0.2156	38.4	0.8	41.8	4.1	527.8	244.4	38.4	0.8	8%
CD316-1-17	1773	1584	1.1	0.0327	0.0027	0.0056	0.0001	0.2247	36.1	0.7	32.7	2.7			36.1	0.7	10%
CD316-1-18	711	429	1.7	0.0346	0.0056	0.0058	0.0002	0.1751	37.1	1.1	34.5	5.5			37.1	1.1	8%
CD316-1-19	1609	2026	0.8	0.0420	0.0035	0.0054	0.0001	0.2225	34.7	0.6	41.8	3.5	553.7	197.2	34.7	0.6	17%
CD316-1-20	780	710	1.1	0.0419	0.0051	0.0060	0.0002	0.2221	38.3	1.0	41.7	5.0	527.8	276.7	38.3	1.0	8%
CD323																	
CD323-1-1	484	142	3.4	0.3028	0.0150	0.0425	0.0005	0.2389	268.1	3.1	268.5	11.7	283.4	118.5	268.1	3.1	0%
CD323-1-2	1026	125	8.2	1.3077	0.0306	0.1398	0.0013	0.4051	843.5	7.5	849.1	13.5	857.4	50.0	843.5	7.5	1%
CD323-1-3	5841	374	15.6	0.6305	0.0113	0.0745	0.0004	0.3307	463.0	2.7	496.4	7.1	635.2	37.0	463.0	2.7	7%
CD323-1-4	2615	2145	1.2	0.0429	0.0033	0.0055	0.0001	0.1854	35.6	0.5	42.7	3.2	524.1	174.8	35.6	0.5	17%
CD323-1-5	1102	156	7.1	1.2674	0.0260	0.1380	0.0009	0.3313	833.4	5.3	831.2	11.6	820.4	44.4	833.4	5.3	0%
CD323-1-6	845	644	1.3	1.1804	0.0254	0.1281	0.0010	0.3499	777.0	5.5	791.5	11.9	827.8	45.5	777.0	5.5	2%
CD323-1-7	128	79	1.6	0.2684	0.0420	0.0202	0.0006	0.2025	129.2	4.1	241.4	33.6	1620.7	294.0	129.2	4.1	46%
CD323-1-8	533	397	1.3	0.9399	0.0321	0.0992	0.0009	0.2722	609.6	5.4	672.8	16.8	887.0	68.5	609.6	5.4	9%
CD323-1-9	3993	77	51.6	0.7509	0.0153	0.0874	0.0011	0.5931	540.2	6.3	568.7	8.9	679.6	37.0	540.2	6.3	5%
CD323-1-10	1612	1715	0.9	0.0315	0.0029	0.0052	0.0001	0.1998	33.7	0.6	31.5	2.8			33.7	0.6	7%
CD323-1-11	1561	963	1.6	1.0661	0.0226	0.1194	0.0013	0.5098	727.1	7.4	736.8	11.1	761.1	39.7	727.1	7.4	1%
CD323-1-12	2036	177	11.5	1.2449	0.0225	0.1355	0.0009	0.3682	819.1	5.1	821.1	10.2	833.3	37.0	819.1	5.1	0%
CD323-1-13	1927	511	3.8	0.8840	0.0189	0.1003	0.0008	0.3520	615.9	4.4	643.2	10.2	738.9	44.4	615.9	4.4	4%
CD323-1-14	2270	1326	1.7	0.0350	0.0027	0.0053	0.0001	0.1897	33.8	0.5	34.9	2.6	189.0	177.8	33.8	0.5	3%
CD323-1-15	1655	1054	1.6	0.1878	0.0077	0.0234	0.0004	0.4586	149.2	2.8	174.7	6.6	531.5	76.8	149.2	2.8	15%
CD323-1-16	612	728	0.8	0.6277	0.0237	0.0780	0.0012	0.3987	484.2	7.0	494.6	14.8	553.7	76.8	484.2	7.0	2%
CD323-1-18	4982	2712	1.8	0.0361	0.0018	0.0055	0.0001	0.2203	35.4	0.4	36.0	1.7	105.6	114.8	35.4	0.4	2%
CD323-1-19	904	678	1.3	0.8523	0.0208	0.1015	0.0008	0.3287	622.9	4.8	625.9	11.4	635.2	49.1	622.9	4.8	0%
CD323-1-20	4678	12	####	0.0301	0.0017	0.0051	0.0001	0.2214	32.7	0.4	30.1	1.7			32.7	0.4	9%
CD325																	
CD325-1-1	2028	4147	0.5	0.6883	0.0167	0.0842	0.0006	0.3110	521.0	3.8	531.8	10.0	572.3	58.3	521.0	3.8	2%
CD325-1-2	1788	772	2.3	1.2091	0.0335	0.1219	0.0012	0.3631	741.8	7.1	804.8	15.4	966.4	47.2	741.8	7.1	8%
CD325-1-3	5851	329	17.8	1.0207	0.0188	0.1145	0.0009	0.4171	698.8	5.1	714.2	9.5	750.0	38.1	698.8	5.1	2%
CD325-1-4	1073	1449	0.7	4.4102	0.0835	0.3031	0.0021	0.3601	1706.7	10.3	1714.2	15.7	1710.8	35.2	1706.7	10.3	0%
CD325-1-5	307	392	0.8	0.2959	0.0273	0.0389	0.0007	0.1965	245.9	4.4	263.2	21.4	501.9	207.4	245.9	4.4	7%
CD325-1-6	6189	5120	1.2	0.1922	0.0087	0.0159	0.0002	0.2476	101.8	1.1	178.5	7.4	1358.3	80.3	101.8	1.1	43%
CD325-1-7	817	700	1.2	1.4828	0.0416	0.1470	0.0013	0.3066	884.1	7.1	923.4	17.0	1005.6	57.4	884.1	7.1	4%
CD325-1-8	955	1342	0.7	1.1198	0.0288	0.1180	0.0012	0.4030	719.3	7.1	762.9	13.8	900.0	57.4	719.3	7.1	6%
CD325-1-9	345	533	0.6	1.4278	0.0937	0.0438	0.0010	0.3316	276.5	5.9	900.6	39.2	3047.8	95.2	276.5	5.9	69%
CD325-1-10	6070	935	6.5	2.1298	0.0467	0.1834	0.0017	0.4311	1085.4	9.5	1158.5	15.2	1264.8	35.7	1085.4	9.5	6%
CD325-1-11	3021	6603	0.5	0.0437	0.0035	0.0056	0.0001	0.1917	36.0	0.5	43.4	3.4	505.6	177.6	36.0	0.5	17%
CD325-1-12	1917	2803	0.7	0.0555	0.0045	0.0058	0.0001	0.1995	37.5	0.6	54.8	4.4	925.0	166.7	37.5	0.6	32%
CD325-1-13	7102	4390	1.6	0.7384	0.0203	0.0781	0.0005	0.2438	485.0	3.1	561.5	11.9	855.2	56.3	485.0	3.1	14%
CD325-1-14	313	504	0.6	0.2714	0.0197	0.0378	0.0006	0.2013	239.1	3.4	243.8	15.8	342.7	169.4	239.1	3.4	2%

CD325-1-15	1614	3570	0.5	0.8492	0.0214	0.0978	0.0008	0.3071	601.3	4.5	624.2	11.8	687.1	53.7	601.3	4.5	4%
CD325-1-16	477	912	0.5	0.2829	0.0151	0.0378	0.0006	0.3012	239.4	3.8	253.0	11.9	420.4	127.8	239.4	3.8	5%
CD325-1-17	2654	3075	0.9	0.3044	0.0082	0.0430	0.0004	0.3075	271.2	2.2	269.9	6.3	253.8	67.6	271.2	2.2	0%
CD325-1-18	228	277	0.8	0.3973	0.0186	0.0386	0.0006	0.3082	244.3	3.5	339.7	13.6	1094.4	100.0	244.3	3.5	28%
CD325-1-19	804	678	1.2	1.4524	0.0367	0.1502	0.0012	0.3173	902.3	6.8	910.9	15.2	920.4	47.2	902.3	6.8	1%
CD325-1-20	1163	431	2.7	1.2839	0.0304	0.1438	0.0012	0.3658	866.3	7.0	838.6	13.5	762.7	51.1	866.3	7.0	3%
CD327																	
CD327-1-1	551	300	1.8	0.2682	0.0133	0.0359	0.0005	0.2898	227.4	3.2	241.2	10.6	376.0	114.8	227.4	3.2	6%
CD327-1-2	309	221	1.4	0.2506	0.0190	0.0359	0.0006	0.2177	227.3	3.7	227.0	15.4	276.0	177.8	227.3	3.7	0%
CD327-1-3	2052	296	6.9	1.1287	0.0222	0.1225	0.0011	0.4380	745.1	6.1	767.1	10.6	816.7	38.9	745.1	6.1	3%
CD327-1-4	732	391	1.9	1.1503	0.0292	0.1228	0.0012	0.3694	746.4	6.6	777.4	13.8	861.1	54.8	746.4	6.6	4%
CD327-1-5	559	493	1.1	0.3512	0.0156	0.0403	0.0005	0.2590	254.5	2.9	305.6	11.7	744.5	98.9	254.5	2.9	17%
CD327-1-6	1634	219	7.5	1.1003	0.0240	0.1246	0.0011	0.4014	756.8	6.3	753.5	11.6	727.8	46.3	756.8	6.3	0%
CD327-1-7	324	182	1.8	0.2465	0.0189	0.0353	0.0006	0.2129	223.9	3.6	223.7	15.4	320.4	185.2	223.9	3.6	0%
CD327-1-8	782	289	2.7	0.2688	0.0118	0.0390	0.0006	0.3318	246.5	3.5	241.7	9.4	198.2	97.2	246.5	3.5	2%
CD327-1-9	293	143	2.0	0.3256	0.0224	0.0420	0.0006	0.2175	265.4	3.9	286.2	17.1	472.3	155.5	265.4	3.9	7%
CD327-1-10	304	223	1.4	0.2152	0.0197	0.0361	0.0006	0.1723	228.6	3.5	197.9	16.4			228.6	3.5	15%
CD327-1-11	2725	380	7.2	0.9329	0.0172	0.1058	0.0008	0.3910	648.2	4.4	669.2	9.0	727.8	39.7	648.2	4.4	3%
CD327-1-12	1046	864	1.2	0.0521	0.0056	0.0061	0.0001	0.1931	39.0	0.8	51.6	5.4	731.5	231.5	39.0	0.8	24%
CD327-1-13	348	249	1.4	0.2241	0.0196	0.0374	0.0005	0.1673	236.7	3.4	205.3	16.3			236.7	3.4	15%
CD327-1-14	447	255	1.8	0.3021	0.0180	0.0434	0.0006	0.2239	273.6	3.6	268.0	14.0	242.7	137.0	273.6	3.6	2%
CD327-1-15	796	625	1.3	0.2625	0.0120	0.0358	0.0004	0.2445	226.5	2.5	236.7	9.7	353.8	105.5	226.5	2.5	4%
CD327-1-16	1284	606	2.1	0.2667	0.0097	0.0387	0.0004	0.2759	244.9	2.4	240.1	7.8	187.1	115.7	244.9	2.4	2%
CD327-1-17	1210	752	1.6	1.1901	0.0259	0.1337	0.0011	0.3755	809.0	6.2	796.0	12.0	766.7	245.4	809.0	6.2	2%
CD327-1-18	1043	198	5.3	1.0494	0.0228	0.1178	0.0010	0.3734	718.1	5.5	728.6	11.3	753.7	44.4	718.1	5.5	1%
CD327-1-19	1223	569	2.1	0.3219	0.0119	0.0439	0.0004	0.2404	277.1	2.4	283.3	9.1	338.9	83.3	277.1	2.4	2%
CD327-1-20	733	368	2.0	0.2715	0.0129	0.0375	0.0004	0.2297	237.4	2.6	243.9	10.3	338.9	111.1	237.4	2.6	3%
CD330																	
CD330-1-1	1776	558	3.2	1.4761	0.0285	0.1481	0.0010	0.3446	890.2	5.5	920.6	11.7	988.6	38.9	890.2	5.5	3%
CD330-1-2	905	393	2.3	0.1823	0.0088	0.0223	0.0004	0.4148	142.4	2.8	170.1	7.6	694.5	128.5	142.4	2.8	16%
CD330-1-3	3233	2733	1.2	8.4031	0.1312	0.4114	0.0022	0.3502	2221.5	10.3	2275.5	14.3	2315.7	20.8	2221.5	10.3	2%
CD330-1-4	7040	455	15.5	4.9598	0.0803	0.2995	0.0018	0.3636	1688.7	8.8	1812.5	13.7	1950.0	28.4	1688.7	8.8	7%
CD330-1-5	6261	409	15.3	4.8644	0.0889	0.2941	0.0022	0.4080	1662.0	11.0	1796.1	15.4	1946.3	29.8	1662.0	11.0	7%
CD330-1-6	1101	397	2.8	1.1849	0.0289	0.1262	0.0010	0.3238	766.1	5.7	793.6	13.4	864.8	51.9	766.1	5.7	3%
CD330-1-7	566	493	1.1	0.4897	0.0225	0.0640	0.0007	0.2246	400.2	4.0	404.7	15.4	442.6	99.1	400.2	4.0	1%
CD330-1-8	4155	3006	1.4	8.0144	0.1854	0.3930	0.0034	0.3737	2136.8	15.8	2232.6	20.9	2322.2	37.7	2136.8	15.8	4%
CD330-1-9	7219	476	15.2	4.9904	0.0993	0.2998	0.0019	0.3113	1690.2	9.3	1817.7	16.9	1958.3	34.1	1690.2	9.3	7%
CD330-1-10	2696	1410	1.9	0.5	0.0112	0.0644	0.0005	0.3347	402.3	2.9	410.4	7.6	450.0	17.6	402.3	2.9	2%
CD330-1-11	5867	3937	1.5	8.3841	0.1460	0.4079	0.0032	0.4461	2205.1	14.6	2273.5	15.9	2329.3	32.6	2205.1	14.6	3%
CD330-1-12	5935	481	12.3	5.2788	0.0842	0.3103	0.0019	0.3773	1741.9	9.2	1865.4	13.7	2002.2	26.7	1741.9	9.2	7%
CD330-1-13	6758	8410	0.8	0.2640	0.0060	0.0340	0.0003	0.3352	215.3	1.6	237.9	4.8	477.8	50.0	215.3	1.6	9%
CD330-1-14	3305	1530	2.2	9.1913	0.1693	0.4141	0.0029	0.3839	2233.5	13.4	2357.3	16.9	2464.8	28.5	2233.5	13.4	5%
CD330-1-15	318	204	1.6	0.2503	0.0201	0.0342	0.0006	0.2186	216.8	3.8	226.8	16.4	394.5	187.0	216.8	3.8	4%
CD330-1-16	899	798	1.1	0.0453	0.0049	0.0056	0.0001	0.2075	36.3	0.8	44.9	4.7	633.0	242.6	36.3	0.8	19%
CD330-1-17	400	231	1.7	0.3441	0.0195	0.0414	0.0006	0.2441	261.3	3.5	300.3	14.7	650.0	124.1	261.3	3.5	13%
CD330-1-18	9753	701	13.9	4.9415	0.0740	0.3009	0.0018	0.4022	1696.0	9.0	1809.4	12.7	1935.5	25.6	1696.0	9.0	6%
CD330-1-19	2733	981	2.8	0.0767	0.0037	0.0094	0.0001	0.2280	60.4	0.7	75.0	3.5	561.1	105.5	60.4	0.7	20%
CD330-1-20	602	253	2.4	0.2913	0.0142	0.0369	0.0004	0.2467	233.8	2.8	259.6	11.2	524.1	111.1	233.8	2.8	10%
CD331																	
CD331-2-1	1000	345	2.9	0.2735	0.0106	0.0386	0.0004	0.2741	243.8	2.5	245.5	8.4	276.0	88.0	243.8	2.5	1%
CD331-2-2	4329	3071	1.4	0.0573	0.0025	0.0057	0.0001	0.2611	36.8	0.4	56.6	2.4	1020.4	91.5	36.8	0.4	35%

CD331-2-3	2178	2073	1.1	0.0726	0.0044	0.0060	0.0001	0.2186	38.3	0.5	71.2	4.1	1402.8	118.1	38.3	0.5	46%
CD331-2-4	3542	3166	1.1	0.0459	0.0025	0.0058	0.0001	0.2329	37.0	0.5	45.6	2.4	553.7	122.2	37.0	0.5	19%
CD331-2-5	1153	216	5.3	1.3154	0.0289	0.1349	0.0011	0.3622	815.9	6.1	852.5	12.7	942.6	44.1	815.9	6.1	4%
CD331-2-6	884	608	1.5	0.0448	0.0065	0.0056	0.0001	0.1532	35.7	0.8	44.5	6.3	635.2	346.1	35.7	0.8	20%
CD331-2-7	597	406	1.5	0.3698	0.0213	0.0375	0.0006	0.2562	237.1	3.4	319.5	15.8	950.0	114.8	237.1	3.4	26%
CD331-2-8	862	208	4.1	0.3024	0.0143	0.0390	0.0004	0.2136	246.7	2.5	268.3	11.2	461.2	103.7	246.7	2.5	8%
CD331-2-9	796	471	1.7	0.0738	0.0076	0.0059	0.0002	0.2596	38.0	1.0	72.3	7.2	1701.9	223.9	38.0	1.0	47%
CD331-2-10	1985	2071	1.0	0.0560	0.0044	0.0058	0.0001	0.2135	37.0	0.6	55.3	4.3	1044.1	162.8	37.0	0.6	33%
CD331-2-11	4955	2547	1.9	0.0472	0.0021	0.0054	0.0001	0.2848	34.9	0.4	46.8	2.0	750.0	102.8	34.9	0.4	26%
CD331-2-12	802	487	1.6	0.0599	0.0078	0.0056	0.0001	0.1987	35.9	0.9	59.1	7.5	1395.4	265.7	35.9	0.9	39%
CD331-2-13	2532	1582	1.6	0.0394	0.0032	0.0053	0.0001	0.1862	33.9	0.5	39.2	3.1	387.1	185.2	33.9	0.5	14%
CD331-2-14	5450	4762	1.1	0.0336	0.0017	0.0053	0.0001	0.2741	33.9	0.5	33.6	1.6	42.7	118.5	33.9	0.5	1%
CD331-2-15	5423	968	5.6	0.0490	0.0023	0.0068	0.0001	0.2255	43.9	0.5	48.6	2.2	300.1	104.6	43.9	0.5	10%
CD331-2-16	2850	1691	1.7	0.0656	0.0052	0.0056	0.0001	0.1846	36.2	0.5	64.5	5.0	1258.9	154.6	36.2	0.5	44%
CD331-2-17	2009	151	13.3	1.2834	0.0249	0.1304	0.0009	0.3543	790.3	5.1	838.4	11.1	961.1	39.7	790.3	5.1	6%
CD331-2-18	1209	691	1.8	0.0409	0.0047	0.0055	0.0001	0.1409	35.1	0.6	40.7	4.6	450.0	247.2	35.1	0.6	14%
CD331-2-19	1417	366	3.9	0.3743	0.0169	0.0392	0.0004	0.2070	248.1	2.3	322.8	12.5	875.9	87.0	248.1	2.3	23%
CD331-2-20	1339	1181	1.1	0.0427	0.0047	0.0059	0.0001	0.1620	37.7	0.7	42.4	4.6	483.4	254.6	37.7	0.7	11%
CD335-1/CD435-1																	
CD335-1-1	1194	384	3.1	1.7252	0.0310	0.1649	0.0011	0.3731	984.1	6.1	1018.0	11.6	1083.3	30.6	1018.0	11.6	3%
CD335-1-3	1469	265	5.5	1.1206	0.0228	0.1338	0.0009	0.3385	809.6	5.3	763.3	11.0	620.4	42.6	809.6	5.3	6%
CD335-1-4	897	322	2.8	4.7725	0.0849	0.3283	0.0026	0.4379	1830.3	12.4	1780.1	15.0	1714.5	29.9	1780.1	15.0	3%
CD335-1-6	2311	314	7.4	1.0505	0.0221	0.1272	0.0009	0.3397	771.7	5.2	729.1	11.0	598.2	42.6	771.7	5.2	6%
CD335-1-7	942	294	3.2	1.0315	0.0264	0.1293	0.0010	0.3135	783.6	5.9	719.7	13.2	527.8	55.5	783.6	5.9	9%
CD335-1-8	1520	311	4.9	1.0120	0.0237	0.1262	0.0010	0.3225	766.1	5.5	709.9	12.0	538.9	48.1	766.1	5.5	8%
CD335-1-9	1259	181	6.9	0.9721	0.0227	0.1156	0.0012	0.4622	705.0	7.2	689.5	11.7	642.6	46.3	705.0	7.2	2%
CD335-1-10	1624	477	3.4	1.0365	0.0209	0.1245	0.0009	0.3438	756.6	5.0	722.2	10.5	616.7	42.6	756.6	5.0	5%
CD335-1-11	3420	304	11.2	0.4277	0.0095	0.0613	0.0006	0.4103	383.7	3.4	361.6	6.7	216.7	48.1	383.7	3.4	6%
CD335-1-12	2222	349	6.4	1.1468	0.0209	0.1332	0.0008	0.3412	806.0	4.7	775.7	9.9	683.3	38.1	806.0	4.7	4%
CD335-1-13	3332	102	32.5	0.3487	0.0085	0.0470	0.0005	0.4773	296.0	3.4	303.7	6.4	350.1	48.1	296.0	3.4	3%
CD335-1-14	548	663	0.8	1.0572	0.0300	0.1219	0.0010	0.2972	741.5	5.9	732.5	14.8	698.2	63.9	741.5	5.9	1%
CD335-1-15	1301	454	2.9	1.1695	0.0254	0.1292	0.0012	0.4128	783.1	6.6	786.4	11.9	790.7	46.3	783.1	6.6	0%
CD335-1-16	495	209	2.4	0.6517	0.0204	0.0846	0.0008	0.3123	523.8	4.9	509.5	12.5	455.6	75.0	523.8	4.9	3%
CD335-1-17	1774	8	####	0.4903	0.0119	0.0641	0.0005	0.3196	400.2	3.0	405.1	8.1	420.4	53.7	400.2	3.0	1%
CD335-1-18	1044	255	4.1	1.2445	0.0261	0.1346	0.0009	0.3214	813.9	5.2	820.9	11.8	825.6	44.4	813.9	5.2	1%
CD335-1-19	1014	667	1.5	1.1755	0.0270	0.1294	0.0010	0.3284	784.7	5.6	789.2	12.6	787.0	48.9	784.7	5.6	1%
CD335-1-20	1413	424	3.3	1.2181	0.0279	0.1268	0.0009	0.3131	769.8	5.2	808.9	12.8	901.9	48.9	769.8	5.2	5%
CD435-1-1	419	228	1.8	0.0423	0.0026	0.0058	0.0001	0.3774	37.3	0.9	42.1	2.6	427.8	121.3	37.3	0.9	11%
CD435-1-2	281	125	2.2	1.1364	0.0482	0.1378	0.0016	0.2739	832.2	9.1	770.8	22.9	590.8	91.7	832.2	9.1	8%
CD435-1-3	340	77	4.4	1.0862	0.0529	0.1363	0.0015	0.2279	823.6	8.6	746.6	25.7	531.5	114.8	823.6	8.6	10%
CD435-1-14	907	75	12.1	1.0314	0.0397	0.1255	0.0016	0.3330	762.4	9.2	719.6	19.9	583.4	83.3	762.4	9.2	6%
CD435-1-15	395	70	5.6	1.1774	0.0384	0.1408	0.0021	0.4568	849.1	11.9	790.1	17.9	635.2	69.3	849.1	11.9	7%
CD435-1-16	327	47	7.0	1.1457	0.0338	0.1330	0.0017	0.4454	805.0	10.0	775.2	16.0	699.7	63.0	805.0	10.0	4%
CD435-1-17	443	54	8.3	1.2145	0.0322	0.1356	0.0022	0.6102	819.5	12.4	807.3	14.8	783.3	53.7	819.5	12.4	2%
CD435-1-18	318	84	3.8	1.1136	0.0279	0.1250	0.0014	0.4465	759.1	8.0	759.9	13.4	761.1	52.9	759.1	8.0	0%
CD435-1-19	300	53	5.7	1.3047	0.0315	0.1392	0.0018	0.5494	840.4	10.4	847.8	13.9	873.8	45.4	840.4	10.4	1%
CD435-1-21	345	60	5.7	1.2496	0.0306	0.1326	0.0021	0.6321	802.8	11.7	823.2	13.8	887.0	80.6	802.8	11.7	2%
CD435-1-22	565	111	5.1	0.9750	0.0224	0.1068	0.0014	0.5632	654.1	8.0	691.1	11.5	803.4	47.2	654.1	8.0	5%
CD435-1-24	862	152	5.7	1.1934	0.0281	0.1256	0.0015	0.5113	762.8	8.7	797.5	13.0	900.0	47.1	762.8	8.7	4%
CD435-1-26	515	103	5.0	1.1952	0.0264	0.1282	0.0015	0.5363	777.4	8.7	798.4	12.2	857.4	45.5	777.4	8.7	3%
CD435-1-28	433	79	5.5	1.2929	0.0287	0.1330	0.0018	0.6154	805.2	10.3	842.6	12.7	946.3	43.1	805.2	10.3	4%
CD435-1-29	204	73	2.8	1.2868	0.0357	0.1385	0.0021	0.5391	836.2	11.7	839.9	15.9	870.1	59.3	836.2	11.7	0%

CD435-1-30	447	79	5.7	1.2303	0.0273	0.1286	0.0014	0.4787	780.1	7.8	814.5	12.4	905.6	44.4	780.1	7.8	4%
CD435-1-31	385	255	1.5	0.3062	0.0114	0.0397	0.0005	0.3597	251.2	3.3	271.2	8.9	438.9	83.3	251.2	3.3	7%
CD435-1-32	332	73	4.6	1.5409	0.0383	0.1506	0.0017	0.4562	904.1	9.6	946.9	15.3	1042.6	48.6	904.1	9.6	5%
CD435-1-33	208	83	2.5	8.3802	0.1888	0.4153	0.0054	0.5718	2239.3	24.4	2273.0	20.5	2299.7	36.4	2273.0	20.5	1%
CD435-1-36	541	82	6.6	1.3323	0.0272	0.1414	0.0017	0.5974	852.5	9.8	859.9	11.9	883.3	44.4	852.5	9.8	1%
CD435-1-37	425	88	4.8	1.3843	0.0298	0.1462	0.0017	0.5363	879.9	9.5	882.3	12.7	900.0	77.9	879.9	9.5	0%
CD435-1-39	396	69	5.8	1.3293	0.0314	0.1413	0.0017	0.5197	852.0	9.8	858.6	13.7	872.2	44.0	852.0	9.8	1%
CD435-1-40	567	93	6.1	1.2748	0.0297	0.1369	0.0017	0.5455	827.1	9.9	834.5	13.3	847.8	152.8	827.1	9.9	1%
CD435-1-41	167	135	1.2	2.6526	0.0732	0.2297	0.0034	0.5407	1332.7	18.0	1315.4	20.4	1300.0	53.4	1315.4	20.4	1%
CD435-1-44	403	70	5.7	1.2468	0.0331	0.1326	0.0024	0.6868	802.6	13.8	821.9	15.0	887.0	53.7	802.6	13.8	2%
CD435-1-45	233	93	2.5	1.2766	0.0380	0.1329	0.0019	0.4898	804.2	11.0	835.3	17.0	920.4	65.7	804.2	11.0	4%
CD435-1-46	366	87	4.2	1.2720	0.0313	0.1332	0.0018	0.5550	806.1	10.4	833.3	14.0	905.6	56.5	806.1	10.4	3%
CD435-1-47	354	70	5.1	1.2307	0.0342	0.1327	0.0021	0.5758	803.2	12.1	814.7	15.6	861.1	61.1	803.2	12.1	1%
CD435(2)-1-2	59	47	1.3	0.2816	0.0166	0.0419	0.0006	0.0141	264.3	3.8	251.9	13.1	198.2	137.0	264.3	3.8	5%
CD435(2)-1-4	161	94	1.7	0.0304	0.0042	0.0056	0.0001	0.0021	36.3	0.9	30.4	4.1			36.3	0.9	20%
CD435(2)-1-6	306	72	4.3	1.1843	0.0190	0.1313	0.0012	0.0413	795.0	6.9	793.3	8.9	794.4	34.3	795.0	6.9	0%
CD435(2)-1-7	98	58	1.7	0.0438	0.0052	0.0055	0.0001	0.0017	35.1	0.9	43.5	5.1	683.3	266.6	35.1	0.9	19%
CD435(2)-1-8	749	853	0.9	0.0335	0.0014	0.0055	0.0001	0.0018	35.1	0.4	33.4	1.3			35.1	0.4	5%
CD435(2)-1-9	531	533	1.0	0.0383	0.0018	0.0054	0.0001	0.0017	34.5	0.6	38.2	1.8	366.7	104.6	34.5	0.6	10%
CD435(2)-1-10	170	117	1.5	0.0377	0.0037	0.0055	0.0001	0.0019	35.5	0.7	37.6	3.7	205.6	225.9	35.5	0.7	5%
CD435(2)-1-12	178	118	1.5	0.0345	0.0034	0.0054	0.0001	0.0017	34.9	0.7	34.4	3.4	77.9	220.3	34.9	0.7	1%
CD435(2)-1-13	160	97	1.6	0.0437	0.0041	0.0059	0.0001	0.0020	37.8	0.7	43.4	4.0	435.2	213.9	37.8	0.7	13%

Note: Ages were accepted with up to 10% and 20% discordance for plutonic and volcanic samples, respectively. All errors are at the 1-sigma level.

Table S3 Zircon U-Pb geochronologic ages for Mesozoic magmatic rocks exposed within the LZTB, SE Tibet.

Location	Sample ID	Longitude (E)	Latitude (N)	Lithology	Formation	Age type	Age (Ma)	± (Ma)	Reference
Weixi	CD144	99.5151	27.0599	granite	Tgr	Zircon U-Pb	227.7	4.6	This study
Weixi	CD149	99.4999	27.0996	granite	Tgr	Zircon U-Pb	234.5	4.7	This study
Jianchuan	CD327	99.6304	26.6027	dacite	Pantiange Fm.($T_{1\text{-}2}p$)	Zircon U-Pb Weigthed mean age of youngest concordant zircons (7 ages)	234.4	8.5	This study
Jianchuan	CX036-8	99.6646	26.5578	granite	Tgr	Zircon U-Pb	244.9	2.2	Yang et al., 2014
Jianchuan	CX037-10	99.6765	26.5671	granite	Tgr	Zircon U-Pb	244.9	2.2	Yang et al., 2014
Jianchuan	QD-2	99.5082	26.7703	dacite	Pantiange Fm.($T_{1\text{-}2}p$)	Zircon U-Pb	244.9	3.3	Yang et al., 2014
Jianchuan	QD-5	99.5082	26.7703	dacite	Pantiange Fm.($T_{1\text{-}2}p$)	Zircon U-Pb	236.9	2.8	Yang et al., 2014
Jianchuan	DX038-2	99.6860	26.5533	volcanoclastic	Pantiange Fm.($T_{1\text{-}2}p$)	U/Pb Weigthed mean age of youngest concordant zircons (14 ages)	246.5	6.3	Yang et al., 2014
Maliqing	D2047-3	99.6834	26.4501	dacite	Pantiange Fm.($T_{1\text{-}2}p$)	Zircon U-Pb	247.0	4.3	Tang et al.,2016
Maliqing	D3052-1	99.6835	26.4501	rhyolite	Pantiange Fm.($T_{1\text{-}2}p$)	Zircon U-Pb	250.0	4.3	Tang et al.,2016
Maliqing	D3053-1	99.7000	26.4501	rhyolite	Pantiange Fm.($T_{1\text{-}2}p$)	Zircon U-Pb	246.7	4.3	Tang et al.,2016
Maliqing	D3055-5A	99.7001	26.4667	rhyolitic lava	Pantiange Fm.($T_{1\text{-}2}p$)	Zircon U-Pb	244.0	5.2	Tang et al.,2016

References

Yang, T. N., Liang, M. J., Fan, J. W., Shi, P. L., Zhang, H. R., and Hou, Z. H., 2014, Paleogene sedimentation, volcanism, and deformation in eastern Tibet: Evidence from structures, geochemistry, and zircon U-Pb dating in the Jianchuan Basin, SW China: Gondwana Research, v. 26, no. 2, p. 521-535.

Tang, L., Xue, C., Yang, T., Liang, M., Xiang, K., Liao, C., Jiang, L., and Xin, D., 2016, Late Permian to Early Triassic tectonostratigraphy of Madeng area, northwestern Yunnan, S.W. China: Volcanics zircon U-Pb dating: Acta Petrologica Sinica, no. 8, p. 2535-2554.

Table S4 Geochronologic ages for Eocene volcanic clasts and plutonic rocks in and around the Jianchuan basin and LZTB, SE Tibet.

Location	Sample ID	Longitude (E)	Latitude (N)	Lithology	Formation	Age type	Age (Ma)	± (Ma)	Reference
Within the Ludian-Zhonghejiang fold-thrust belt									
Laojun Shan	CD316	99.6712	26.5934	Porphyry		Zircon U-Pb weigthed mean age of the youngest concordant zircons (10 ages)	34.5	1.3	This study
Laojun Shan	CD323	99.6616	26.6113	Granitic porphyry		Zircon U-Pb weigthed mean age of the youngest concordant zircons (5 ages)	34.3	1.6	This study
Laojun Shan	CD325	99.6420	26.6105	Granite		Zircon U-Pb age of the only youngest age (1 age)	36.0	0.5	This study
Laojun Shan	CD330	99.6248	26.6014	Granitic porphyry		Zircon U-Pb age of the only youngest age (1 age)	36.3	0.8	This study
Laojun Shan	CD335/CD435	99.6991	26.5534	Lamprophyre		Zircon U-Pb weigthed mean age of the youngest concordant zircons (6 ages)	35.1	0.5	This study
Laojun Shan	CD331	99.6171	26.6010	Granitic porphyry		Zircon U-Pb weigthed mean age of the youngest concordant zircons (6 ages)	35.3	1.7	This study
Laojun Shan	CD321-1	99.6713	26.6175	Granitic porphyry		Zircon U-Pb weigthed mean age of the youngest concordant zircons (12 ages)	34.7	0.8	Gourbet et al., 2017
Jianchuan basin interstratified (Jianchan Fm.(E_2jc))									
Jianchuan basin	J161	99.8919	26.5913	Volcanoclastics	Jianchuan Fm.(E_2jc)	Zircon U-Pb lower intercept of the youngest population (3 ages)	35.9	1.1	Gourbet et al., 2017
Jianchuan basin	J284	99.8509	26.6324	Rhyolitic tuff	Jianchuan Fm.(E_2jc)	Zircon U-Pb lower intercept of the youngest population (3 ages)	34.8	1.1	Gourbet et al., 2017
Laojun Shan	J308	99.6484	26.4346	Volcanoclastics	Jianchuan Fm.(E_2jc)	Zircon U-Pb weigthed mean age of the youngest concordant zircons (4 ages)	35.0	2.3	Gourbet et al., 2017
Laojun Shan	DX-39-5	99.6113	26.5082	Volcanoclastics	Jianchuan Fm.(E_2jc)	Zircon U-Pb weigthed mean age of the youngest concordant zircons (4 ages)	34.7	0.2	Yang et al., 2014
Jianchuan basin interstratified (Shuanghe Fm.(E_2s))									
Jianchuan basin	J121	99.8672	26.4477	Trachy-andesitic lava flow	Shuanghe Fm.(E_2s)	Zircon U-Pb lower intercept of the main population (22 ages)	35.8	0.3	Gourbet et al., 2017
Jianchuan basin	J120	99.8672	26.4477	Trachy-andesitic lava flow	Shuanghe Fm.(E_2s)	Zircon U-Pb lower intercept of the youngest grain (2 ages)	35.0	1.0	Gourbet et al., 2017
Jianchuan basin	J168A	99.8529	26.5970	Volcanoclastic	Shuanghe Fm.(E_2s)	Zircon U-Pb lower intercept of the main population (34 ages)	35.7	0.2	Gourbet et al., 2017
Jianchuan basin	J278	99.8770	26.5918	Volcanoclastic	Shuanghe Fm.(E_2s)	Zircon U-Pb age of the only youngest age (1 age)	36.8	1.0	Gourbet et al., 2017
Jianchuan basin	J203	99.8531	26.5904	Volcanic tuff	Shuanghe Fm.(E_2s)	Zircon U-Pb lower intercept of the youngest zircons (18 ages)	36.4	0.4	Gourbet et al., 2017
Jianchuan basin	DX-030-6	99.8672	26.4477	Trachydacite volcanic level	Shuanghe Fm.(E_2s)	Zircon U-Pb weigthed mean age of the youngest concordant zircons (18 ages)	36.6	0.7	Yang et al., 2014
Jianchuan basin	JIAN-11-06	99.8531	26.5904	Ttuffaceous sandstone	Shuanghe Fm.(E_2s)	Zircon U-Pb weigthed mean age of the youngest concordant zircons (5 ages)	37.1	1.6	Hoke et al., 2014
Plutonic rocks around the Jianchuan county									
Jianchuan (S808)	J279	99.9030	26.5923	Lamprophyre (dyke)		Ar/Ar inverse isochron	34.5	1.0	Gourbet et al., 2017
Jianchuan (Shamao Shan)	JC-9	99.9197	26.5842	Amphibole syenite		Zircon U-Pb	35.6	0.3	Lu et al., 2012
Jianchuan (~8 km east of the Laoiun Shan)	JC-7	99.8121	26.6567	Biotite monzogranite porphyry		Zircon U-Pb	35.3	0.4	Lu et al., 2012
Jianchuan (Laojun Shan)	JC-1	99.7253	26.6323	Amphibole syenite		Zircon U-Pb	35.4	0.2	Lu et al., 2012
Jianchuan (~8 km northeast of the Laojun Shan)	SG-12	99.7764	26.7819	Monzogranite porphyry		Zircon U-Pb	35.7	0.2	Lu et al., 2012
Jianchuan (Laojun Shan)	Y81-791	99.6873	26.7243	Quartz monzonite		Zircon U-Pb	34.5	0.3	Liang et al., 2007
Jianchuan (~10 km north of the Laojun Shan)	Y81-909	99.6944	26.8417	Syenite, monzonite		Zircon U-Pb	35.6	0.2	Liang et al., 2007
~5 km to the east of Jianchuan	Y81-862	99.9000	26.3667	Trachyte		Zircon U-Pb	34.4	0.4	Liang et al., 2007
Jianchuan (Shamao Shan)	YU70			Monzonitic-syenitic		Zircon U-Pb	35.0	0.1	Schärer et al., 1994
Plutonic rocks away from the Jianchuan county									
Midu Gap	Y83-803	100.2889	25.2236	Quartz monzonite porphyry		Zircon U-Pb	34.8	0.3	Liang et al., 2007
Yongping-Weishan	WS-4	100.2870	25.1545	Quartz monzonite porphyry		Zircon U-Pb	35.4	0.6	Lu et al., 2012
Machangqing	BXC-8	100.4258	25.5278	Biotite amphibole monzogranite		Zircon U-Pb	35.6	0.3	Lu et al., 2012
Machangqing	BXC-2	100.4519	25.5341	Amphibole monzogranite porphyry		Zircon U-Pb	35.0	0.2	Lu et al., 2012
Machangqing	BXC-9	100.4258	25.5278	Granitic aplite		Zircon U-Pb	34.4	0.2	Lu et al., 2012
Binchuan	BC-4	100.6568	25.7736	Biotite quartz monzonite porphyry		Zircon U-Pb	35.4	0.4	Lu et al., 2012
Binchuan	BC-5	100.4763	25.7926	Amphibole quartz monzonite porphyry		Zircon U-Pb	36.6	0.6	Lu et al., 2012
Beiya	72ZK11-207			Monzogranite porphyry		Zircon U-Pb	36.9	0.3	Lu et al., 2012
Beiya	BY-9	100.1804	26.1462	Alkali feldspar granite porphyry		Zircon U-Pb	36.2	0.3	Lu et al., 2012
Beiya	56ZK14-4			Alkali feldspar syenite porphyry		Zircon U-Pb	34.6	0.5	Lu et al., 2012
Beiya	BY-YKD	100.1845	26.1628	Biotite monzogranite porphyry		Zircon U-Pb	36.8	0.7	Lu et al., 2012
Beiya	TKT	100.2042	26.1640	Monzonite porphyry		Zircon U-Pb	36.9	0.7	Lu et al., 2012
Beiya	LH-1	100.3294	26.4522	Biotite–amphibole–augite syenite porphyry		Zircon U-Pb	36.9	0.3	Lu et al., 2012
Beiya	PTS	100.1864	26.2873	Quartz monzonite porphyry		Zircon U-Pb	36.5	0.8	Lu et al., 2012
Beiya	BL-2	100.2257	26.1478	Monzogranite porphyry		Zircon U-Pb	35.7	0.8	Lu et al., 2012
Yao'an	YA-2	101.2891	25.3853	Biotite quartz monzonite porphyry		Zircon U-Pb	33.4	0.3	Lu et al., 2012
Yongsheng-Ninglang	DHS-1	100.9860	26.8467	Biotite quartz monzodiorite porphyry		Zircon U-Pb	33.1	0.4	Lu et al., 2012
Yongsheng-Ninglang	DHS-4	100.9742	26.8595	Biotite granite porphyry		Zircon U-Pb	34.1	0.3	Lu et al., 2012
Yongsheng-Ninglang	BNC-3	100.9307	27.3614	Granite porphyry		Zircon U-Pb	32.5	0.3	Lu et al., 2012
~100 km east of Midu	Y81-974	101.2528	25.3833	Trachydacite		Zircon U-Pb	34.0	0.5	Liang et al., 2007
~25 km east of Xiaguan	Y83-634	100.4292	25.5250	Syenite, quartz monzonite		Zircon U-Pb	35.5	0.4	Liang et al., 2007
~25 km east of Xiaguan	Y83-620	100.4319	25.5194	Quartz monzonite porphyry		Zircon U-Pb	34.8	0.2	Liang et al., 2007
~25 km south of CD100	Y83-745	100.2028	26.1125	Quartz monzonite porphyry		Zircon U-Pb	35.6	0.5	Liang et al., 2007
~25 km south of CD101	Y83-740	100.2333	26.1631	Quartz monzonite porphyry		Zircon U-Pb	35.7	0.6	Liang et al., 2007
~25 km south of CD102	Y83-760	100.1722	26.3000	Quartz monzonite porphyry		Zircon U-Pb	36.2	0.6	Liang et al., 2007
Phan Si Pan	YS50	103.7744	22.3646	Syenite, quartz monzonite		Zircon U-Pb	35.0	0.3	Zhang and Schärrer, 1999
Phan Si Pan	Sh-126	103.1292	22.7500	Syenite, quartz monzonite		Zircon U-Pb	35.4	0.4	Liang et al., 2007
Phan Si Pan	Y81-78	103.0583	22.7917	Granitic pporphyry, quartz monzonite porphyry		Zircon U-Pb	35.1	0.3	Liang et al., 2007

References

Gourbet, L., Leloup, P. H., Paquette, J., Sorrel, P., Maheo, G., Wang, G., Yadong, X., Cao, K., Antoine, P., Eymard, I., Liu, W., Lu, H., Replumaz, A., Chevalier, M., Kexin, Z., Jing, W., and Shen, T., 2017, Reappraisal of the Jianchuan Cenozoic basin stratigraphy and its implications on the SE Tibetan plateau evolution: Tectonophysics, v. 700-701, no. Supplement C, p. 162-179.

Hoke, G. D., Liu-Zeng, J., Hren, M. T., Wissink, G. K., and Garzione, C. N., 2014, Stable isotopes reveal high southeast Tibetan Plateau margin since the Paleogene: Earth and Planetary Science Letters, v. 394, no. 0, p. 270-278.

Liang, H. Y., Campbell, I. H., Allen, C. M., Sun, W. D., Yu, H. X., Xie, Y. W., and Zhang, Y. Q., 2007, The Age of the Potassic Alkaline Igneous Rocks along the Ailao Shan‐Red River Shear Zone: Implications for the Onset Age of Left‐Lateral Shearing: The Journal of Geology, v. 115, no. 2, p. 231-242.

Liu, Y., Hu, Z., Gao, S., Günther, D., Xu, J., Gao, C., and Chen, H., 2008, In situ analysis of major and trace elements of anhydrous minerals by LA-ICP-MS without applying an internal standard: Chemical Geology, v. 257, no. 1–2, p. 34-43.

Lu, Y., Kerrich, R., Cawood, P. A., McCuaig, T. C., Hart, C. J. R., Li, Z., Hou, Z., and Bagas, L., 2012, Zircon SHRIMP U–Pb geochronology of potassic felsic intrusions in western Yunnan, SW China: Constraints on the relationship of magmatism to the Jinsha suture: Gondwana Research, v. 22, no. 2, p. 737-747.

Schärer, U., Zhang, L., and Tapponnier, P., 1994, Duration of strike-slip movements in large shear zones: The Red River belt, China: Earth and Planetary Science Letters, v. 126, no. 4, p. 379-397.

Yang, T. N., Liang, M. J., Fan, J. W., Shi, P. L., Zhang, H. R., and Hou, Z. H., 2014, Paleogene sedimentation, volcanism, and deformation in eastern Tibet: Evidence from structures, geochemistry, and zircon U-Pb dating in the Jianchuan Basin, SW China: Gondwana Research, v. 26, no. 2, p. 521-535.

Zhang, L., and Schärer, U., 1999, Age and origin of magmatism along the Cenozoic Red River shear belt, China: Contributions to Mineralogy and Petrology, v. 134, no. 1, p. 67-85.

Table S5 Zircon and apatite (U-Th)/He data.

Sample	Aliq.	He		U		Th		Th/U	grain mass (μg)	Ejection corr. (F_T238)	Ejection corr. (F_T235)	Ejection corr. (F_T232)	Rs (μm)	[U] (ppm)	[Th] (ppm)	[eU] (ppm)	Uncorr. He age (Ma)	F_T-Corr. He age (Ma)	1σ (Ma)	Weighted mean age (Ma)	1σ(Ma)
		vol. (ncc)	1σ (%)	mass (ng)	1σ (%)	mass (ng)	1σ (%)														
Zircon																					
CD144	z1	2.532	0.053	4.772	0.068	1.278	0.018	0.275	2.39	0.742	0.706	0.706	46.47	1422.94	381.13	1512.51	91.88	124.02	3.10	121.37	1.93
	z2	2.717	0.057	5.000	0.071	1.082	0.015	0.222	4.17	0.778	0.746	0.746	54.55	895.89	193.94	941.47	95.15	122.46	3.06		
	z3	1.349	0.029	2.530	0.036	0.693	0.010	0.281	5.04	0.785	0.754	0.754	56.46	345.25	94.55	367.47	92.17	117.63	2.94		
CD145	z1	1.686	0.035	3.982	0.057	1.372	0.020	0.354	1.83	0.726	0.687	0.687	43.45	1537.76	529.91	1662.29	72.24	99.87	2.48	107.68	4.68
	z2	2.343	0.049	5.078	0.072	1.479	0.021	0.299	2.49	0.745	0.708	0.708	46.95	1425.89	415.39	1523.50	79.58	107.14	2.67		
	z3	1.842	0.039	3.703	0.052	1.428	0.020	0.396	1.83	0.726	0.688	0.688	43.56	1312.19	505.96	1431.09	84.00	116.04	2.87		
CD148	z1	2.757	0.058	5.254	0.075	1.696	0.024	0.331	0.04	0.760	0.725	0.725	50.18	1172.58	378.46	1261.52	89.81	118.46	2.94	119.42	7.27
	z2	2.312	0.049	5.558	0.079	1.532	0.022	0.283	0.03	0.714	0.673	0.673	41.41	1989.97	548.64	2118.90	72.04	101.26	2.52		
	z3	1.709	0.036	3.023	0.043	0.874	0.012	0.297	0.03	0.714	0.673	0.673	41.41	1124.88	325.28	1201.33	97.39	136.77	3.42		
	z4	5.956	0.125	10.255	0.146	4.762	0.068	0.476	0.08	0.797	0.767	0.767	60.14	1248.12	579.57	1384.32	96.33	121.18	2.99		
Apatite																					
CD145	*a1	0.000	0.000	0.135	0.002	0.173	0.002	1.307	2.41	0.726	0.689	0.689	51.92	43.57	55.52	56.62	0.06	0.09	0.01	35.85	3.2
	a2	0.012	0.000	0.089	0.001	0.110	0.002	1.263	1.41	0.675	0.632	0.632	42.96	47.07	57.93	60.68	19.57	29.40	0.41		
	a3	0.017	0.000	0.087	0.001	0.104	0.001	1.223	1.33	0.647	0.601	0.601	39.17	55.45	66.09	70.98	27.78	43.58	0.64		
	a4	0.019	0.000	0.056	0.001	0.343	0.005	6.320	5.08	0.796	0.768	0.768	71.37	7.61	46.87	18.62	24.96	31.97	0.44		
	a6	0.034	0.000	0.150	0.002	0.253	0.004	1.725	4.84	0.775	0.743	0.743	64.06	26.26	44.16	36.64	29.47	38.43	0.48		
CD148	a1	0.035	0.000	0.120	0.002	0.222	0.003	1.889	4.25	0.756	0.723	0.723	58.95	24.01	44.20	34.40	37.06	49.59	0.73	41.67	2.58
	*a2	0.002	0.000	0.127	0.002	0.246	0.004	1.991	4.37	0.762	0.730	0.730	60.54	24.30	47.16	35.38	1.81	2.40	0.06		
	a3	0.019	0.000	0.089	0.001	0.172	0.002	1.991	2.51	0.710	0.671	0.671	48.72	28.57	55.44	41.60	27.59	39.48	0.57		
	a4	0.014	0.000	0.074	0.001	0.134	0.002	1.865	2.28	0.697	0.656	0.656	46.37	29.07	52.86	41.49	24.73	36.07	0.59		
	a5	0.021	0.000	0.098	0.001	0.198	0.003	2.079	3.30	0.726	0.689	0.689	51.93	22.89	46.39	33.79	26.79	37.45	0.50		
	a6	0.021	0.000	0.085	0.001	0.166	0.002	2.007	2.11	0.682	0.640	0.640	44.00	36.42	71.26	53.17	30.65	45.78	0.61		

* Ages were deemed outliers based on Dixon's q-test (https://en.wikipedia.org/wiki/Dixon%27s_Q_test), and not used for weight mean age calculation and inverse modeling.

Table S6 Apatite fission-track data.

Sample ID	N_g[a]	Track number	Density	U[b]	$P(\chi^2)$[c]	Dispersion	Pooled age	± 1σ	Length[d]	± 1σ	N_l[e]	D_{par}	D_{per}
			(10^5 cm^{-2})	(ppm)	(%)	(%)	(Ma)	(Ma)	(μm)	(μm)		(μm)	(μm)
CD144	40	946	21.99	16.46	43	0.31	35.8	2.8	13.93	1.29	169	2.15	0.36
CD146	39	872	15.87	13.35	56	0.03	45.3	3.7	13.74	1.56	171	2.15	0.36
CD147	40	852	17.00	13.38	55	0.47	41.3	3.4	13.35	1.72	161	2.00	0.35
CD148	40	841	17.91	12.08	66	0.00	38.7	3.2	14.01	1.41	162	2.03	0.35
CD149	40	930	17.42	13.29	65	0.01	44.0	3.5	13.50	1.48	161	1.99	0.37

a Number of grains analyzed.
b Average uranium content of all crystals measured using LA-ICP-MS.
c Chi-square value for υ degrees of freedom (υ=N-1).
d Track length measured after 252Cf irradiation, and projected in respect to c axis (Ketchem et al., 2007).
e Number of track length measured.
Note: Zeta value is 8.27266 ± 0.1407.

1156